TURUN YLIOPISTO
UNIVERSITY OF TURKU

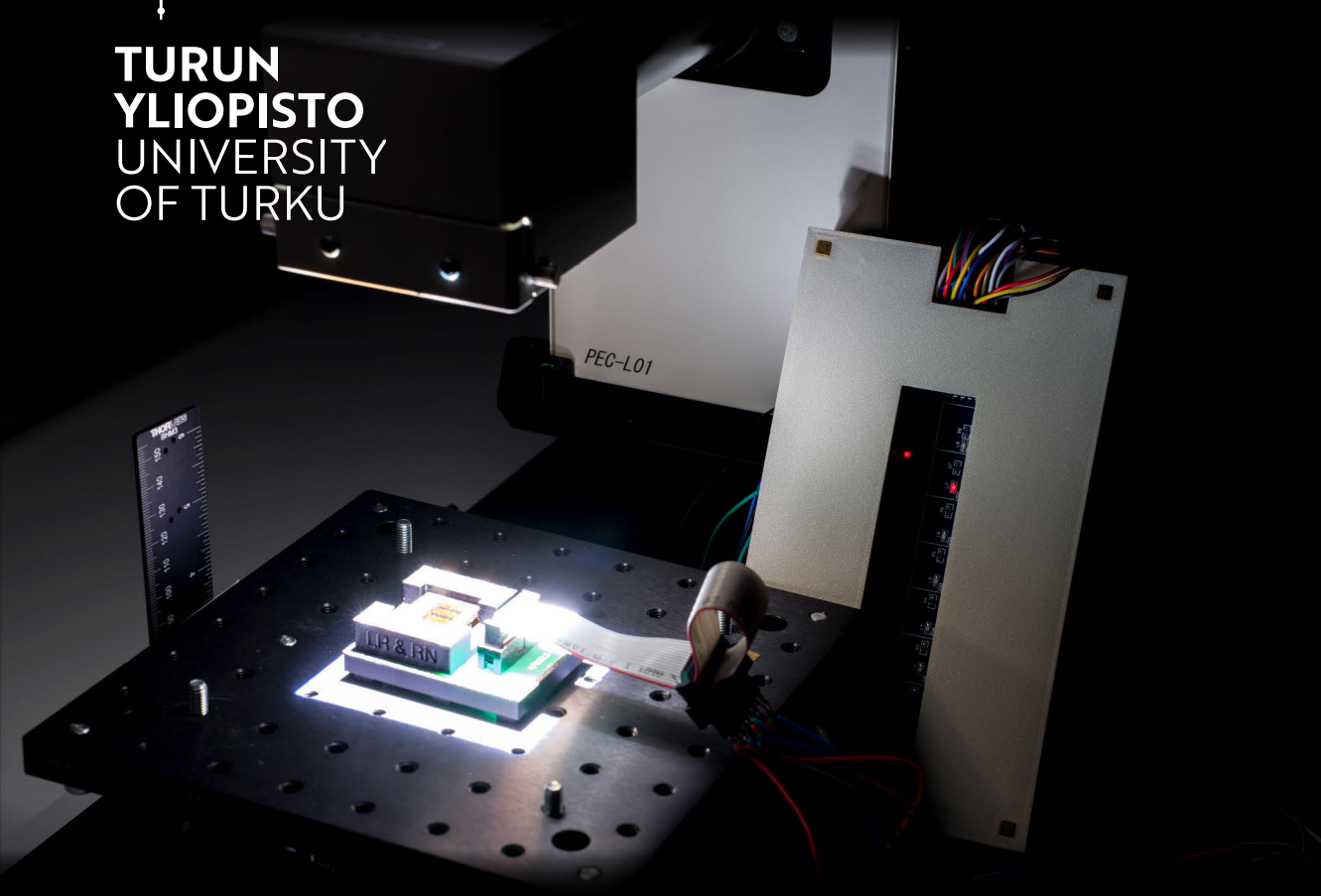

Stability Testing of Sustainable Materials for Photovoltaic Applications

Rustem Nizamov

TURUN YLIOPISTON JULKAISUJA – ANNALES UNIVERSITATIS TURKUENSIS
SARJA – SER. F OSA – TOM. 62 | TECHNICA – INFORMATICA | TURKU 2025

TURUN
YLIOPISTO
UNIVERSIT
OF TURKU

STABILITY TESTING OF SUSTAINABLE MATERIALS FOR PHOTOVOLTAIC APPLICATIONS

Rustem Nizamov

TURUN YLIOPISTON JULKAISUJA – ANNALES UNIVERSITATIS TURKUENSIS
SARJA – SER. F OSA – TOM. 63 | TECHNICA – INFORMATICA | TURKU 2025

University of Turku

Faculty of Technology
Department of Mechanical and Materials Engineering
Materials Engineering
The Doctoral Programme in Technology

Supervised by

Professor, Kati Miettunen
University of Turku

D.Sc. (Tech.), Aapo Poskela
University of Turku

Reviewed by

D.Sc. (Tech.), Hannes Orelma
VTT-Technical Research Centre of Finland

Professor, Arri Priimägi
Tampere University

Opponent

Associate Professor, Francesca Brunetti
University of Rome "Tor Vergata"

The originality of this publication has been checked in accordance with the University of Turku quality assurance system using the Turnitin OriginalityCheck service.

Cover Image: Rustem Nizamov

ISBN 978-952-02-0327-6 (PRINT)
ISBN 978-952-02-0328-3 (PDF)
ISSN 2736-9390 (PRINT)
ISSN 2736-9684 (ONLINE)
Painosalama Oy, Turku, Finland, 2025

To my family, whose unwavering support and boundless love have been my shelter through all these years. Without you, I would never have found my inspiration.

Җир яшәрмәс, гөл ачылмас — төшми яңгыр тамчысы;
Кайдан алсын шигъре шагыйрь, булмаса илһамчысы.
— Габдулла Тукай

UNIVERSITY OF TURKU
Faculty of Technology
Department of Mechanical and Materials Engineering
Materials Engineering
NIZAMOV, RUSTEM: Stability Testing of Sustainable Materials for Photovoltaic Applications
Doctoral dissertation, 165 pp.
The Doctoral Programme in Technology
August 2025

ABSTRACT

Sustainable materials hold great promise for photovoltaic and other photoresponsive applications; their long-term performance, however, is significantly affected by ultraviolet (UV)-induced degradation and other environmental stressors. This thesis investigates the stability and degradation mechanisms of various sustainable materials and devices—nanocellulose (NC)-based films, zinc oxide (ZnO)-coated textiles, dye-sensitized solar cells (DSSCs), and perovskite solar cells (PSCs)—under various conditions. A consistent, non-invasive, color-based method was used to assess degradation, providing insights into material performance and durability over time.

The research on NC-based films targeted their optical performance, particularly their UV-shielding properties, achieved by incorporating sustainable additives like lignin and red onion (*Allium cepa*) extract. While bio-based UV filters have demonstrated promising initial results, their long-term effectiveness remains unexplored. To address this gap, extended aging tests were conducted to evaluate their capacity to provide sustained UV protection over time. This color-based assessment was also explored in photovoltaic devices, including DSSCs and PSCs, where color alterations were correlated with electrical performance changes. While color alteration and degradation occurred concurrently in PSCs, electrolyte color changes in DSSCs offered a predictive tool for degradation, potentially accelerating stability research. The study also investigated ZnO-coated textiles for their UV-blocking and photocatalytic self-cleaning capabilities. Furthermore, to address challenges in PSC research where substrate etching introduces variability, a tunable-design additive-manufactured holder was developed.

The color-based technique, applied across these diverse studies, proved robust and cost-effective for tracking material changes and monitoring stability. Observed color alterations consistently served as an indicator of degradation, correlating with changes in optical and electrical properties across various materials. These findings contribute to advancing durable, eco-friendly materials and establishing scalable methods for stability assessment.

KEYWORDS: Sustainability, stability, color alteration, photovoltaics, optoelectronics, UV protection, nanocellulose, perovskite solar cells

TURUN YLIOPISTO
Teknillinen tiedekunta
Kone- ja materiaalitekniikan laitos
Materiaalitekniikka
NIZAMOV, RUSTEM: Stability Testing of Sustainable Materials for Photovoltaic Applications
Väitöskirja, 165 s.
Teknologian tohtoriohjelma
Elokuu 2025

TIIVISTELMÄ

Uusiutuvat materiaalit ovat lupaavia aurinkosähkö- ja muissa valoherkissä sovelluksissa, mutta niiden pitkäaikainen suorituskyky kärsii ultraviolettisäteilyn (UV) aiheuttamasta hajoamisesta ja muista ympäristön aiheuttamista rasitteista. Tässä väitöskirjassa tutkitaan uusiutuvien materiaalien ja uuden sukupolven laitteiden – nanoselluloosapohjaisten kalvojen (NC), sinkkioksidilla (ZnO) päällystettyjen tekstiilien, väriaineherkistettyjen aurinkokennojen (DSSCs) ja perovskiittiaurinkokennojen (PSCs) – stabiilisuutta ja hajoamisprosesseja erilaisissa olosuhteissa. Hajoamista arvioitiin ei-invasiivisella, väriin perustuvalla menetelmällä, joka antoi tietoa materiaalien suorituskyvystä ja kestävyydestä ajan mittaan.

NC-pohjaisten kalvojen tutkimuksessa keskityttiin kalvojen optisiin ominaisuuksiin, erityisesti UV-suojausominaisuuksiin, jotka saavutettiin lisäämällä kalvoihin uusiutuvia lisäkomponenteja, kuten ligniiniä ja punasipulin (*Allium cepa*) uutetta. Vaikka biopohjaiset UV-suodattimet ovat alustavasti osoittaneet lupaavia tuloksia, niiden pitkäaikainen tehokkuus on vielä tutkimatta. Tämän selvittämiseksi suoritettiin ikäännyttämistestejä, joissa arvioitiin biopohjaisten UV-suodattimien kykyä tarjota UV-suojaa. Tätä väriin perustuvaa arviointia tutkittiin aurinkosähkökennoissa, kuten DSSC- ja PSC-kennoissa, joissa värimuutokset korreloivat sähköisten suorituskykyjen muutosten kanssa. Vaikka PSC-kennoissa värimuutokset ja hajoaminen tapahtuivat samanaikaisesti, niin DSSC-kennojen elektrolyytin värimuutokset tarjosivat työkalun ennustamaan ja arvioimaan hajoamisen, mikä voi nopeuttaa stabiilisuustutkimusta. Tutkimuksessa perehdyttiin ZnO-pinnoitettujen tekstiilien UV-suojaus- ja fotokatalyyttisiä itsepuhdistusominaisuuksia. Lisäksi kehitettiin lisäävällä valmistuksella pidike PSC-tutkimuksen haasteiden ratkaisemiseksi tilanteissa, joissa substraatin etsaus aiheuttaa vaihtelevuutta.

Näissä tutkimuksissa sovellettu väripohjainen analysointitekniikka osoittautui luotettavaksi ja kustannustehokkaaksi materiaalimuutosten seurannassa ja vakauden valvonnassa. Havaitut värimuutokset toimivat johdonmukaisesti hajoamisen indikaattoreina, ja ne korreloivat eri materiaalien optisten ja sähköisten ominaisuuksien muutosten kanssa. Nämä havainnot edistävät kestävien, ympäristöystävällisten materiaalien kehittämistä ja vakauden arviointia varten sovellettavien laskennallisten menetelmien luomista.

ASIASANAT: Kestävyys, stabiilisuus, värimuutos, aurinkosähkö, optoelektroniikka, UV-suoja, nanoselluloosa, perovskiittiaurinkokenno

Acknowledgements

What you are holding is not merely a book, but the culmination of years of research, learning, and persistence, all of which have flowed into these pages as structured knowledge. This complex journey could never have been accomplished through individual effort alone. On the contrary, it is only through the profound support of many people and organizations that this work has been brought to fruition. I wish to express my deepest gratitude to all who have contributed to this dissertation and to my growth as a researcher.

First and foremost, I extend my sincere appreciation to my primary supervisor, Professor Kati Miettunen. Your insightful guidance, unwavering support, and consistent encouragement have been fundamental throughout my doctoral studies. I am also deeply grateful to my second supervisor, Dr. Aapo Poskela. Your valuable input, constructive feedback, and expert advice have been instrumental in shaping this research. I would also like to thank the pre-examiners of this dissertation, Dr. Hannes Orelma and Professor Arri Priimägi, for their thorough review and constructive feedback. My sincere appreciation also goes to my opponent, Associate Professor Francesca Brunetti, for her valuable time and scholarly engagement with this work. This work was generously supported by the Finnish National Agency for Education, the Tandem Forest Values programme, the Finnish Cultural Foundation, and the Research Council of Finland.

This research was a collaborative effort, and I want to express my deepest thanks to Dr. Joice Kaschuk. Her expertise, guidance, and cheerful meetings made it possible for me to overcome my fears and dive deep into a new field for me. I am also grateful for the opportunity to work with Professors Tiffany Abitbol, Jaana Vapaavuori, Monika Österberg, Orlando Rojas and Dr. Karl Alexander Henn, Dr. Rafael Grande, and Dr. Yazan Al Haj. Your input and advice were undoubtedly essential for my journey.

Next, I want to extend my gratitude to Joaquín Valdez García. Thank you for the countless coffee breaks, the "fancy lunches," and for making the daily grind of PhD life so much more enjoyable. To Maryam Esmaeilzadeh, our soulful conversations over coffee meant a lot to me. To Alicja Lawrynowicz, thank you for your patience and friendship, and to Emilia Palo, for conversations that always left a warm feeling in my heart. To Dr. Mahboubeh Hadadian, thank you for your sincere discussions and endless positivity (focus, focus, focus).

A special thank you goes to Mikael Nyberg, whose mentorship and expertise as a lab engineer have been invaluable. I also extend my sincere thanks to the entire support team, especially Helen Salminen, Akseli Nykänen, and Teemu Hynnä. Your assistance, patience, and good humor made all the difference.

To all current and past members of the SEMS group: Dr. Sami Jouttijärvi, Aleksi Kamppinen, Elena Akulenko, Julianna Varjopuro, Helmi Vuorinen, Tytti Jusuti, Väinö Anttalainen, Kimmo Pyyhtiä, and many more. Words cannot describe what our time together, both inside and outside of work, has meant to me. I also wish to thank many other researchers for their support and valuable discussions, including Dr. Hamidreza Daghigh Shirazi, Dr. Pedro Santo Silva, Dr. Eduardo Martínez, Dr. Jerzy Jasielec, Dr. Henri Lyyra, Dr. Ransell D'Souza, Dr. Nianxing Wang, Michael A. Papachatzakis, Dr. Gabriel Gonzalez, Dr. Jenna Hannonen, Dr. Sari Granroth, Ahmed Abdelmagid, Hassan Qureshi, Oskar Tuomi, Ali Tuna, Reza Akhtari, Mohammad Fatemi, and countless others to whom I am deeply grateful. If I have forgotten to mention anyone here, please forgive my poor memory. I am also grateful to all the staff and teaching personnel of our department for their valuable advice and knowledge sharing!

To Dr. Manish Kumar, your friendship has been one of the most cherished aspects of my PhD experience. Thank you for being a true friend and for your unwavering support. I also wish to extend my heartfelt thanks to my dear friends Dr. Andrei Morariu and Lauri Karttunen. Our cycling adventures and shared moments have been a wonderful part of this journey. I also want to warmly thank Dr. Artem Plyusnin, and his family. Your friendship has been a constant source of support through the most challenging times and the most joyful milestones.

I extend my deepest love and gratitude to my family back home. To my parents and my dear aunts in the Yaña Chüpräle, thank you for always believing in me and for laying the foundation that made this journey possible. Your support, even from afar, has been a constant in my life.

And finally, to the two people who have been my inspiration, and my most steadfast support: my beloved wife, Regina, and my wonderful son, Rafael. Regina, your unwavering love, patience, understanding, and belief in me have been the foundation upon which this work rests. You have shouldered so much to allow me the space and time to pursue this, and your encouragement during the most challenging moments was often the only thing that kept me going. Thank you for being my rock, my partner, and my everything. To my dear son, Rafael, you have brought so much joy and meaning to my life. Seeing your smile always reminds me of what truly matters. This achievement is dedicated to you both. Without your love and sacrifice, none of this would have been possible, nor would it have meant half as much.

September 11, 2025
Rustem Nizamov

Table of Contents

Abbreviations

3D three-dimensional

AI artificial intelligence

AM air mass

Au-PSC gold electrode perovskite solar cell

BSK bleached softwood kraft pulp

C-PSC carbon electrode perovskite solar cell

CIE Commission Internationale de l'Éclairage

CIELAB CIE 1976 $L^*a^*b^*$ color space

CIELCh CIE $L^*C^*h^\circ$ color space

CLP colloidal lignin particles

CME carbon monolithic electrode

CMY cyan, magenta, and yellow color space

CNC cellulose nanocrystals

CNF cellulose nanofibers

CNF-LNP CNF with lignin nanoparticles (produced according to the **publication I**)

CNF-LNP GDE coated CNF film with colloidal lignin particles deposition (produced according to the **publication II**)

CNF-ROE CNF film dyed with red onion (*Allium cepa*) dye

D65 CIE standard illuminant representing average daylight

DIN German Institute for Standardisation

DIN99 DIN99 color difference equation

DNG digital negative

DSSC dye-sensitized solar cell

EIS electrical impediation spectroscopy

FESEM field-emission scanning electron microscopy

FTO fluorine-doped tin oxide

ISOS International Summit on Organic PV Stability

ITO indium tin oxide

IV current-voltage

JV current density-voltage

LED light emitting diode

Ligno-CNF residual lignin containing CNF

Ligno-TOCNF residual lignin containing TOCNF

LNP lignin nanoparticles

MTM sodium montmorillonite clay

NC nanocellulose

opRGB Adobe RGB (1998) color space

PET polyethylene terephthalate

PSC perovskite solar cell

PV photovoltaic

PVC polyvinyl chloride

RGB red, green, and blue

SMU source measure unit

sRGB standard Red Green Blue color space

SRSS square root of the sum of squares

TOCNC TEMPO-mediated oxidized CNC

TOCNF TEMPO-mediated oxidized CNF

TOCNF-ECH Fe^{3+} TEMPO-mediated oxidized CNF film with epichlorohydrin induced chemically-physically crosslinked iron ion (III)

TOCNF-LNP TOCNF with lignin nanoparticles

TOCNF-Fe^{3+} TEMPO-mediated oxidized CNF film with physically crosslinked iron ions (III)

UBSK unbleached softwood kraft pulp

UPF ultraviolet protection factor

UV ultraviolet

UV-Vis-NIR ultraviolet, visible, near-infrared

WVTR water vapor transmission rate

XRD X-ray diffraction

Materials

3MPN 3-methoxypropionitrile

Ag silver

Au gold

Br bromine

C carbon

c-TiO_2 compact TiO_2

CH_3NH_2 methylamine

CH_3NH_3 methylammonium

Cl chlorine

CO_2 carbon dioxide

CsFAMA $Cs_{0.05}(FA_{0.83}MA_{0.17})_{0.95}Pb(I_{0.83}Br_{0.17})_3$

ECH epichlorohydrin

$FeCl_3$ iron(III) chloride

FK209 Tris(2-(1H-pyrazol-1-yl)-4-*tert*-butylpyridine)cobalt(III) tris(bis(trifluoromethanesulfonyl)imide)

GDE glycerol diglycidyl ether

GuSCN guanidinium thiocyanate

H_2SO_4 sulfuric acid

HCl hydrochloric acid

I atomic iodine

I^- iodide ion

I_3^- tri-iodide ion

I_2 molecular iodine

KOH potassium hydroxide

LiTFSI lithium bis(trifluoromethanesulfonyl)imide

$MAPbI_3$ methylammonium lead iodide

MB methylene blue

meso-TiO_2 mesoporous TiO_2

NaBr sodium bromide

NaClO sodium hypochlorite

NaOH sodium hydroxide

NH_4OH ammonium hydroxide

NMBI 1-methylbenzimidazole

Pb lead

PbI_2 lead iodide

PMII 1-propyl-3-methylimidazolium iodide

PVDF polyvinylidene fluoride

Spiro-OMeTAD 2,2',7,7'-Tetrakis[N,N-di(4-methoxyphenyl)amino]-9,9'-spirobifluorene

tBP 4-*tert*-butylpyridine

TEMPO 2,2,6,6-tetramethylpiperidine-1-oxyl radical

THF tetrahydrofuran

$Ti(acac)_2OiPr_2$ Titanium diisopropoxide bis(acetylacetonate)

TiO_2 titanium dioxide

Zn zinc

ZnO zinc oxide

Symbols

R red color component in RGB color space

G green color component in RGB color space

B blue color component in RGB color space

Y yellow color component in CMY color space

L^* CIELAB lightness

a^* CIELAB a^* coordinate

b^* CIELAB b^* coordinate

C^* CIELAB (CIELCh) chroma

h° CIELAB (CIELCh) hue angle

ΔRGB Euclidean distance in the RGB color space

$\sigma_{\Delta RGB}$ standard deviation of the color change vectors

ΔL^* difference between two L^* values

ΔE^*_{ab} CIELAB color difference

ΔE_{DIN99} color difference between two colors given in CIELAB colorspace using DIN99 formula

J_{SC} short-circuit current density

V_{OC} open-circuit voltage

FF fill factor

η power conversion efficiency

I_{lim} limiting current

$D_{I_3^-}$ diffusion coefficient of tri-iodide

$c_{I_3^-}$ concentration of tri-iodide

d distance between electrodes of dye solar cell

F Faraday constant

RH relative humidity

$E(\lambda)$ erythema action spectrum

$S(\lambda)$ solar spectral irradiance

$T(\lambda)$ spectral transmittance of the fabric

$\Delta\lambda$ wavelength interval of the measurements

List of Original Publications

This dissertation is based on the following original publications, which are referred to in the text by their Roman numerals:

I **Rustem Nizamov**, Joice Kaschuk, Yazan Al Haj, Mikael Nyberg, Monireh Imani, Eva Pasquier, Orlando Rojas, Tiffany Abitbol, Jaana Vapaavuori, Kati Miettunen. Optical assessment of lignin-containing nanocellulose films under extended sunlight exposure. *Cellulose*, 2025; 1–14.

II **Rustem Nizamov**, Aapo Poskela, Joice Kaschuk, Karl Alexander Henn, Rafael Grande, Sari Granroth, Mikael Nyberg, Maryam Esmaeilzadeh, Jaana Vapaavuori, Monika Österberg, Kati Miettunen. Sustainable nanocellulose UV filters for photovoltaic applications: Comparison of red onion (*Allium cepa*) extract, iron ions, and colloidal lignin. *ACS Applied Optical Materials*, 2025, 3(3): 664–675.

III Tiffany Abitbol, Mikaela Kubat, Elisabet Brännvall, Nikolay Kotov, C. Magnus Johnson, **Rustem Nizamov**, Mikael Nyberg, Kati Miettunen, Niklas Nordgren, Jasna S. Stevanic, Maria Pita Guerreiro. Isolation of Mixed Compositions of Cellulose Nanocrystals, Microcrystalline Cellulose, and Lignin Nanoparticles from Wood Pulps. *ACS Omega*, 2023; 8(24): 21474–21484.

IV Joaquín Valdez García, Anna Boding, Xuan Yang, **Rustem Nizamov**, Michael S. Reid, Kristina Junel, Kati Miettunen, Tiffany Abitbol, Joice Kaschuk. Multifunctional nanocellulose hybrid films: From packaging to photovoltaics. *International Journal of Biological Macromolecules*, 2025; 292: 139203.

V Alicja Lawrynowicz, Emilia Palo, **Rustem Nizamov**, Kati Miettunen. Self-Cleaning and UV-blocking cotton—fabricating effective ZnO structures for photocatalysis. *Journal of Photochemistry and Photobiology A: Chemistry*, 2024; 450: 115420.

VI Joaquín Valdez García, Mahboubeh Hadadian, **Rustem Nizamov**, Paavo Mäkinen, Noora Lamminen, Paola Vivo, Kati Miettunen. Simplifying perovskite solar cell fabrication for materials testing: how to use unetched

substrates with the aid of a three-dimensionally printed cell holder. *Royal Society Open Science*, 2024; 11(9): 241012.

VII **Rustem Nizamov**, Aapo Poskela, Mahboubeh Hadadian, Maryam Esmaeilzadeh, Mikael Nyberg, Kati Miettunen. Analysis of color alteration as a novel degradation assessment method for perovskite solar cells. *Proceedings of the EU PVSEC 2024*, 2024; 020083-001–020083-006.

The original publications have been reproduced with the permission of the copyright holders.

Related publication by the author not included in the thesis:

- Elena S. Akulenko, Mahboubeh Hadadian, Maryam Esmaeilzadeh, **Rustem Nizamov**, Kati Miettunen. Bottlenecks in perovskite solar cell recycling. *Proceedings of the EU PVSEC 2023*, 2023; 020106-001–020106-004.
- Mahboubeh Hadadian, Thomas W. Gries, G. Krishnamurthy Grandhi, Emil Rosqvist, **Rustem Nizamov**, Sari Granroth, Paola Vivo, Ronald Österbacka, Jan-Henrik Smått, Antonio Abate, Kati Miettunen. The Role of Terminal Functional Groups on Molecular Passivation of the Perovskite/Hole-Selective Layer Interface. *SUBMITTED*.

Declaration of AI use

In preparing this dissertation, generative artificial intelligence (AI) features in PyCharm 2025.1.1.1 were used only for grammar, spelling, readability, and LaTeX formatting. No AI was used to develop research concepts, analyze data, or draw conclusions.

Author's contribution

Throughout each project, the doctoral candidate's core responsibilities encompassed running the aging tests, designing and operating the photographic setup, and extracting quantitative color metrics to evaluate degradation processes. These activities provided a consistent methodological framework, unifying the dissertation's focus on non-invasive color-based diagnostics. All materials and device samples in the publications featured in this dissertation were prepared by internal and external collaborators.

In the publications **I**, **II**, and **VII**, where the doctoral candidate was the first author or shared first authorship, the candidate was responsible for writing the manuscript, with input from all co-authors. Additionally, the doctoral candidate conducted the aging experiments and related data acquisitions and performed the subsequent data analysis and visualization.

Within the other studies—**III**, **IV**, and **V** —the doctoral candidate similarly carried out the aging experiments, photographic documentation, and quantitative color analysis. The candidate's manuscript contributions in these cases were primarily focused on sections describing experimental findings and color-based stability assessments. Across all these collaborations, the doctoral candidate consistently provided essential input to ensure that color measurement and stability insights were accurately reported.

A notable exception is the **publication VI**, where the candidate designed and fabricated a three-dimensional printed holder to facilitate simplified perovskite solar cell characterization, eliminating the requirement for electrode etching. The doctoral candidate also contributed to writing the methodology section of this manuscript.

1 Introduction

Our planet is facing a global warming crisis, to which human activities have significantly contributed.[1] This climate change is linked to the increasing levels of carbon dioxide (CO_2) and other greenhouse gases in the atmosphere.[2] Given the urgency of this issue, immediate action is necessary to mitigate its long-term consequences.

One of the most practical strategies to combat global warming is the widespread adoption of renewable energy sources as an alternative to conventional fossil fuels.[3] The transition to renewable energy has underscored the importance of sustainable materials in photovoltaic (PV) and optoelectronic applications. Bio-based materials, in particular, have emerged as a promising alternative – offering eco-friendly solutions for PV technologies[4] as well as for a wide range of applications such as packaging and sensors.[5,6] Despite all potential environmental benefits, bio-based materials' long-term stability remains a critical challenge. In particular, ultraviolet (UV) light exposure has been identified as a key factor in compromising both performance and material reliability.[7]

In light of these challenges, this dissertation aims to evaluate the stability of sustainable materials under various aging conditions, with an emphasis on degradation mechanisms induced by UV light. The research evaluates nanocellulose (NC)-based materials (also known as cellulose nanomaterials, featured in the publications **I–IV**) modified for enhanced durability and UV-blocking functionality, including the application of predictive stability modeling for dye-sensitized solar cells (DSSCs) based on colorimetric data in the **publication II**. The **publication V** examines UV-driven self-cleaning textiles (zinc oxide (ZnO)-coated cotton). Furthermore, this work extends to perovskite solar cells (PSCs)—**publication VI** and **publication VII** —focusing on fabrication improvements (using unetched substrates) and long-term stability assessments.

A central theme of this dissertation is the development and application of a non-invasive, color-alteration-based monitoring technique. This approach was used both to track material degradation over time and to deepen insights into the degradation processes of these materials and devices. The method was first applied to NC films, then extended to textiles, and finally implemented in PV devices, consistently linking material color change with performance degradation. By leveraging this approach, this work presents a unified and scalable strategy for real-time stability monitoring across multiple classes of sustainable optoelectronic materials.

2 Background

2.1 Nanocellulose

Cellulose is a naturally abundant and renewable polysaccharide, widely used in sustainable applications due to its biodegradability, biocompatibility, and low cost.[8,9] Owing to its ready availability, straightforward processing, and modifiability, cellulose has found extensive use as a sustainable substrate across numerous fields, including packaging, optoelectronics, and printable electronics.[10,11] One compelling class of cellulose-based materials is known as NC – a collective term for high-aspect-ratio fibrous or rod-like structures derived from cellulose. Furthermore, the scalability of NC manufacturing methods adds to its appeal. Unlike materials such as glass, which require processing at extremely high temperatures (1200–1600°C) with substantial CO_2 emissions, cellulose can be produced at comparatively low temperatures and with reduced carbon (C) footprints.[12–15]

NC is often classified into two primary categories. Cellulose nanofibers (CNF) are characterized by fibrillar structures spanning various size scales, with the finest fibrils having widths of 3–4 nm and lengths of hundreds of nanometers, sometimes coexisting with microscale fibrillar bundles; they typically form stronger, more flexible films.[16] In contrast, cellulose nanocrystals (CNC) present as shorter, more uniform rod-like structures with widths of 5–10 nm and lengths under 500 nm, higher crystallinity, but lower strain at break.[16] Both CNF and CNC can be processed into dense, transparent films with the capability to modulate light in ways beneficial for advanced applications.[17,18] Moreover, NC-based substrates can be produced in large areas at relatively low cost, supporting emerging flexible electronics and biodegradable packaging solutions.[19]

Neat cellulose itself exhibits poor stability under UV light, as it is susceptible to photo-oxidative degradation.[20] This process is driven by a free-radical mechanism that leads to the formation of chromophores, such as carbonyl groups, and the depolymerization of cellulose chains.[20] A range of analytical techniques can be used to assess these changes: ultraviolet, visible, near-infrared (UV-Vis-NIR) spectroscopy tracks the optical consequences, field-emission scanning electron microscopy (FE-SEM) and X-ray diffraction (XRD) observe morphological alterations. Although the resulting color alteration is a direct manifestation of this degradation, it is often considered only qualitatively or in the context of aesthetics and color stability.

Chemical functionalization enables a richer set of properties in NC films. One notable example is the 2,2,6,6-tetramethylpiperidine-1-oxyl radical (TEMPO) oxidation approach, wherein TEMPO along with sodium hypochlorite (NaClO) and sodium bromide (NaBr) selectively converts primary hydroxyls on cellulose to carboxyl groups.[21] The resulting TEMPO-mediated oxidized CNF (TOCNF) (and TEMPO-mediated oxidized CNC (TOCNC)) can reach higher transparency or better mechanical strength depending on the target application.[22] This enhanced transparency in TOCNF is attributed to the creation of more uniform, finer elemental fibrils, which leads to better dispersion and less light scattering compared to the more heterogeneous fibril structure of unmodified CNF.[23] This carboxyl functionalization allows doping with a range of additives, such as ions or other molecules, for applications such as improved barrier properties, conductive coatings, or UV protection.[24] Yet, even neat unmodified CNF or CNC can be combined with additives to achieve similar functionality.

Sunlight is essential for photovoltaic devices and other optoelectronic applications, yet the UV segment of the spectrum can seriously degrade device components. Because cellulose by itself does not sufficiently absorb harmful UV (in particular UVA[1]) wavelengths, it is pivotal to embed UV-shielding capabilities into NC-based films to ensure stable device operation. Among the promising bio-based strategies, lignin has attracted considerable attention due to its intrinsic UV-absorbing ability, which can be retained from unbleached pulps or introduced as lignin nanoparticles (LNP).[16,25] Similarly, natural anthocyanin dyes extracted from red onion or other agricultural by-products can be coated onto cellulose, forming stable colorants that strongly absorb in the UV range.[26] Beyond optical applications, NC films offer a broad spectrum of other functionalities, such as oxygen barrier properties, tunable swelling, or mechanical reinforcement, which can be further enhanced by combining NC with layered nanoclays or forming hybrid composites.[27] Though the target properties may differ between fields, NC's inherent customizability and low environmental impact make it a prime candidate for replacing traditional synthetic substrates.

Altogether, these advancements illustrate how doping with lignin, anthocyanins, or ionic cross-linkers can elevate NC beyond conventional applications and enable genuinely biodegradable, high-performance materials for solar cells, flexible electronics, and intelligent packaging. Nevertheless, long-term stability evaluations under intense illumination or real-world conditions remain crucial to fully harness the potential of NC-based films.

[1] UV irradiation includes UVC (100–280 nm), UVB (280–315 nm), and UVA (315–400 nm)

2.2 Photovoltaics

PV technologies are designed to directly convert sunlight into electricity, playing a crucial role in the global shift towards renewable energy sources. Silicon-based panels currently dominate the PV market, but alternative technologies such as DSSCs and PSCs have emerged in recent years.[28,29] In principle, PV devices rely on semiconductor-based absorber layers that capture incident light and convert it into electrical current, with the device's performance and operational lifetime influenced by its design, material quality, and internal interfaces.

Operational lifetime is a key factor in the commercial viability of PV devices. While lifespan expectations differ significantly based on the application, many conventional panel systems aim for reliable function over 20–25 years or more. However, achieving these lifespans is challenging, as many PV materials are vulnerable to degradation from environmental factors, with UV being a notable concern. To evaluate whether novel or modified PV materials can approach this lifetime target, accelerated aging tests are employed, exposing samples to UV radiation, thermal stresses, and humidity under controlled, intensified conditions. In crystalline silicon-based devices, well-established procedures such as IEC 61215 have long guided reliability testing,[30] but these standards do not directly translate to new PV technologies with distinct material properties. Accordingly, the International Summit on Organic PV Stability (ISOS) consortium introduced specialized stability-testing protocols, initially tailored for organic solar cells.[31] These guidelines have now been widely adopted by the perovskite community, enabling systematic comparisons of device stability under consistent stress conditions.[32] The assessment of PV degradation is primarily quantified by monitoring the decline of key electrical performance parameters over time under various stressors.[33] This is typically achieved through periodic current-voltage (IV) measurements, which track the evolution of the power conversion efficiency (η), fill factor (FF), open-circuit voltage (V_{OC}), and short-circuit current density (J_{SC}).

2.2.1 Dye-sensitized solar cells

A DSSC is an electrochemical device that converts light energy into electricity through a photoelectrochemical process.[34] Typically arranged in a sandwich architecture, it consists of a porous titanium dioxide (TiO_2) photoanode sensitized by an organometallic or organic dye, an electrolyte containing redox couples (for instance, iodide ion (I^-)/tri-iodide ion (I_3^-)), and a catalytic counter electrode (Figure 1). When visible light excites the dye molecules, electrons are injected into the TiO_2 conduction band and carried toward the photoanode's front contact, while oxidized dye species are regenerated by I^-. A catalytic layer at the counter electrode enables I_3^- reduction, thereby completing the circuit.

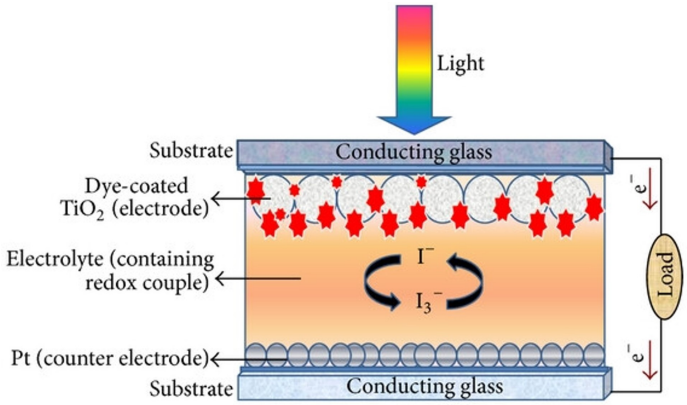

Figure 1. Schematic diagram of a DSSC, illustrating the key components and operating principle. Adapted from Kushwaha et al.[35] under a CC BY 3.0 license.

Thanks to their capability to function under low-intensity or diffuse illumination, DSSCs excel in indoor or portable devices.[36,37] Additionally, roll-to-roll processes can produce patterned modules with customizable color or transparency, expanding design choices across applications.[38,39] Their compatibility with lightweight and flexible plastic substrates makes them highly suitable for emerging applications such as portable and wearable devices.[40] Furthermore, their potential for low production cost, combined with their see-through and colorful properties, expands their design possibilities for a wide range of uses.[40]

The stability challenges for flexible DSSCs stem from the material limitations of their polymer substrates, which include poor thermal stability limiting fabrication options, a high degree of moisture and oxygen penetration, and vulnerability to mechanical stress.[38] However, a more fundamental degradation mechanism common to both flexible and rigid architectures is the intrinsic instability of the electrolyte under UV irradiation. For common iodine-based electrolytes, a primary degradation pathway is the UV-induced photo-oxidation of I^-, a reaction often catalyzed by the TiO_2 surface, which consumes the I_3^- redox mediator.[41,42] Since the I_3^- ion is responsible for the electrolyte's characteristic yellow-brown color, its depletion results in a visible "bleaching" of the cell.[43] This process directly impacts device performance, as the loss of I_3^- reduces the electrolyte's charge-carrying capacity, causing a drop in the limiting current and, consequently, the J_{SC}.[42] While this performance decline is traditionally monitored with electrical characterization methods such as IV measurements and electrical impediation spectroscopy (EIS), the bleaching phenomenon itself presents a unique analytical opportunity. Because the electrolyte's color change typically appears before major performance losses are observed, monitoring this bleaching phenomenon can serve as a practical early indicator of device failure.[44]

2.2.2 Perovskite solar cells

PSCs have garnered significant interest for achieving high power conversion efficiencies (η) with relatively simple, low-temperature fabrication suitable for flexible or otherwise unconventional substrates.[45] A classic PSC comprises an organic–inorganic perovskite layer (of the general form ABX_3, where A and B are cations of different sizes and X is a halogen anion) sandwiched between *n*-type and *p*-type charge-transport layers.[46] For photovoltaics, the larger cation A often is methylammonium (CH_3NH_3), while B is lead (Pb) and X is frequently atomic iodine (I) (sometimes with partial chlorine (Cl) or bromine (Br) substitution). When illuminated, the perovskite absorber generates free charges that are transported through the electron- and hole-selective contacts to external electrodes, creating electrical current.

For the external electrodes, metallic layers such as gold (Au) or silver (Ag) are commonly used as top contacts. However, these metals are susceptible to moisture-induced degradation and can contribute to issues like ion migration.[47,48] As an alternative, carbon-based electrodes (often screen-printed) offer a lower-cost option that can also help mitigate such ion migration. Transparent conductive oxides like indium tin oxide (ITO) or fluorine-doped tin oxide (FTO) are typically used as the bottom contact, also serving as the substrate.

In conventional laboratory-scale research on PSCs, the bottom electrode is deliberately patterned into an array of small "pixels" via chemical or laser etching. A pixel, in the context of solar cells, refers to a single, electrically isolated subcell area with independently addressable contacts, which allows for parallel device testing or modular configurations. This patterning step poses a significant limitation—especially for novel conductive substrates like metallic foils or bio-based materials, where standard etching may be impractical or damaging. Thus, the development of methods that bypass electrode etching can substantially simplify and accelerate PSC research.

Despite their advantages, the operational stability of PSCs is a major challenge, as they are susceptible to degradation from a combination of environmental and intrinsic factors, including moisture, UV light, and heat.[32,33] A primary extrinsic pathway is moisture-induced degradation, where the hygroscopic nature of the organic cation can lead to the decomposition of the perovskite into its precursors, such as non-photoactive lead iodide (PbI_2).[33,49] Similarly, exposure to UV light, particularly in devices using a TiO_2 transport layer, can photocatalytically decompose the perovskite into PbI_2, methylamine (CH_3NH_2), and molecular iodine (I_2), leading to significant performance losses.[33,49] Intrinsic degradation mechanisms also play a critical role, including the migration of mobile ions under electrical bias or heat, which can create defects and react with the metal electrodes, as well as the chemical instability of the charge transport layers themselves.[32,33] A common feature of these degradation pathways is a distinct visual color shift, most notably the change from

the dark brown or black of the active perovskite to the yellow of PbI_2, which serves as a direct indicator of material decomposition and device instability.[33] Addressing such challenges through perovskite composition tuning, interface engineering, and robust encapsulation is an active area of research, aiming to increase operational lifespans under real-world environmental conditions[50]

2.3 Functional textiles

Textiles engineered with novel coatings or embedded active particles have garnered attention for applications ranging from smart wearables to air filtration and self-cleaning surfaces.[51] In particular, hydrophobic and photocatalytic treatments can transform cotton or synthetic fibers into self-cleaning textiles that break down organic stains and microbes when exposed to light. Such coatings often feature metal oxides like TiO_2 or ZnO, which absorb UV photons and facilitate photocatalytic reactions.[52]

The properties of ZnO are thoroughly influenced by the size and shape of its nanostructures.[53] Various synthesis conditions influence coating morphology, thereby impacting the resulting characteristics of the textile fabrics. Depending on the intended application, different geometries such as nanowires, nanorods, or flower-like structures are preferred.[54] Among these, flower-like morphologies have consistently demonstrated enhanced photocatalytic activity due to their elevated surface-to-volume ratios.[55]

Microwave-assisted growth of ZnO nanostructures directly on cotton exemplifies one viable route, producing such flower-like crystals with photocatalytic potential and UV-blocking capability. While promising, these photocatalytic textiles must still withstand prolonged UV exposure, mechanical stress, and repeated wash cycles. This underscores the need for robust design parameters and easy-to-implement diagnostic techniques, such as color-based monitoring, to track coating stability and stain-removal efficiency in real time.

2.4 Fundamentals of color science

Color alteration analysis provides a convenient way to assess complex degradation pathways, particularly when UV exposure or chemical transformations lead to perceptible shifts in hue or opacity. Hue is an attribute of visual perception that describes a color as similar to red, yellow, green, or blue, or a combination of them.[56] Because color changes correlate with underlying photo-oxidation or physical changes, colorimetry – the science of quantifying color – is an appealing choice as a real-time, non-invasive monitoring technique.

Color is a perceptual phenomenon arising from the way the human eye's photoreceptor cells respond to different wavelengths of electromagnetic radiation, typically

within the range of 380–780 nm.[57] Each wavelength corresponds to a particular hue, but the brain's interpretation of color also depends on factors such as ambient illumination (viewing conditions), the object's reflectance spectrum, and adaptation mechanisms within the visual system. In practical applications, color is often quantified using mathematical descriptions known as color spaces, which enable consistent measurements across different devices and viewing conditions.

A color space is a systematic arrangement of coordinates representing perceived colors numerically. For instance, red, green, and blue (RGB) color spaces use three channels (coordinates)—R, G, and B—ranging nominally from 0 to 255 (in 8-bit integer form) or in floating-point representations between 0.0 and 1.0. This three-channel approach is widely adopted in digital imaging because typical camera sensors capture light through red, green, and blue filters, and modern light emitting diode (LED)-based displays use these same primaries to produce images. Although convenient for digital imaging, RGB color spaces are generally device-dependent, meaning the same RGB values can appear as different colors on various uncalibrated devices. They are also not perceptually uniform; a color space is considered perceptually uniform if equal numerical changes in its coordinate values correspond to similarly perceived shifts in color, regardless of the specific color. To address these issues, the Commission Internationale de l'Éclairage (CIE) introduced device-independent color systems designed for better perceptual uniformity, notably the CIE 1976 $L^*a^*b^*$ color space (CIELAB) model characterized by L^*, a^*, and b^*.[57] While L^* is bounded, the a^* and b^* axes are theoretically unbounded; their practical range depends on the reference white and is sufficient to cover the gamut of human color perception. A polar variant of CIELAB is the CIE $L^*C^*h^\circ$ color space (CIELCh) system, where L^* is retained, but a^* and b^* are converted to C^* (chroma, or color intensity) and h° (hue angle), making certain visual relationships more intuitive.

In color science, a color difference quantifies the separation between two colors, offering an objective measure for what would otherwise be subjective descriptions. Among various metrics, the Euclidean distance in CIELAB space ($\Delta {E^*}_{ab}$) is a standard approach for approximate quantification of perceived color shifts.[58] Such calculations assume specific viewing conditions, including the illuminant, a moderate field size (the angular size of the sample to the eye), and chromatic adaptation of the observer to a defined reference white (such as CIE standard illuminant representing average daylight (D65)[59]). This reference white acts as a baseline; accounting for its chromatic adaptation ensures measurements are aligned with how humans perceive colors under specific illumination. Nonetheless, $\Delta {E^*}_{ab}$ values are not perfectly perceptually uniform, since a given $\Delta {E^*}_{ab}$ value might represent a noticeably different perceived difference depending on the specific colors involved. To address these limitations, the German Institute for Standardisation (DIN) DIN99 color difference equation (DIN99) formula refines the difference,[60] introducing ΔE_{DIN99} for improved perceptual uniformity.[61] This formula, before calculating Euclidean dis-

tances, modifies the CIELAB space by mathematically rotating its color axes and applying logarithmic scaling to its coordinates, aiming to follow the Weber-Fechner law of perception.[62] This law states that the just-noticeable difference in a stimulus is proportional to its initial magnitude, meaning human sensory response to a change is logarithmic rather than linear.

When capturing images digitally, device-dependent RGB formats (like standard Red Green Blue color space (sRGB) or Adobe RGB (1998) color space (opRGB)) are most common.[63–65] Such data usually require calibration against a known standard and reference to a specific illuminant to ensure the color information is accurate and comparable across different devices and viewing conditions. This consistency is particularly important when analyzing subtle degradation effects. To overcome the limitations of device-dependent color spaces, RGB data can be converted to a device-independent space like CIELAB. This process typically includes linearizing the RGB data (reversing gamma correction, an adjustment for the non-linear brightness response of displays), potentially applying a chromatic adaptation transform (to account for different illumination or white points), and finally, calculating CIELAB values relative to the chosen reference white.[56,58] Photography-based color characterization has demonstrated high repeatability and reliability, particularly when performed under controlled lighting with consistent exposure settings and by including a color reference chart (a standard target with known color patches).[66] This approach minimizes systematic variations and allows for the accurate correlation of color metrics with material changes over time.

3 Materials and methods

3.1 Materials and devices

3.1.1 Fabrication of nanocellulose-based films

Different NC-based films were prepared for the publications **I–IV**. Specific details for each publication are briefly summarized below.

In the **publication I**, fully bleached and unbleached birch kraft pulps (supplied by Stora Enso, Finland) were fibrillated into CNFs and TOCNFs using high-pressure homogenization. Films (60 g/m^2) were formed by air-pressure filtration, followed by hot-pressing at 30°C.[67] Residual lignin containing CNF (Ligno-CNF) and residual lignin containing TOCNF (Ligno-TOCNF) contained approximately 13–15% lignin, while CNF with lignin nanoparticles (produced according to the **publication I**) (CNF-LNP) and TOCNF with lignin nanoparticles (TOCNF-LNP) had around 9% LNPs.[25,68]

In the **publication II**, NC-based films were prepared with various modifications to achieve UV-blocking functionality:

- CNF film dyed with red onion (*Allium cepa*) dye (CNF-ROE): Birch pulp was fibrillated via high-pressure homogenization, diluted to 1.0g/L, and ultrasonicated for 5 min at 25% amplitude. Films were then formed by vacuum filtration through a polyvinylidene fluoride (PVDF) membrane (0.45 μm pore size) and dried under mild pressure at room temperature for 72 h. The dried CNF films were immersed for 60 min in a red onion (*Allium cepa*) extract, prepared by extracting onion skins in hot water at 80°C for 60 min, producing an anthocyanin-rich solution.[26]

- GDE coated CNF film with colloidal lignin particles deposition (produced according to the **publication II**) (CNF-LNP)[1]: Kraft lignin particles were synthesized by dissolving lignin in a solvent mixture (tetrahydrofuran (THF), ethanol, water), followed by precipitation induced by rapid water addition.[69]

[1] Please note that the materials referred to as **CNF-LNP** in different parts of this thesis—specifically in the **publication I** and **II** —are not fully chemically or structurally identical. Although they share the same naming for consistency and traceability, they differ in formulation and fabrication method as described in Subsection 3.1.1. The naming has been intentionally preserved to align with the respective original publications.

Glycerol diglycidyl ether (GDE) was mixed with colloidal lignin particles (CLP) dispersion (ratio 0.52 g/g). CNF films, pre-coated with glycerol for 10 min to reduce brittleness and enhance uniformity, were coated with the CLP-GDE dispersion using a K-Control Coater (Model 202, green rod, speed 4/10). Films were immediately oven-cured at 105°C for 1 h to achieve better cross-linking and structural stability.

- TEMPO-mediated oxidized CNF film with physically crosslinked iron ions (III) (TOCNF-Fe^{3+}) and TEMPO-mediated oxidized CNF film with epichlorohydrin induced chemically-physically crosslinked iron ion (III) (TOCNF-ECH Fe^{3+}): Films were prepared by filtering TOCNF suspensions.[24,70–72] For TOCNF-Fe^{3+}, wet films were immersed in a 1 mol/L iron(III) chloride ($FeCl_3$) solution for 24 h, rinsed, and hot-pressed at 30°C (1 kg/m² pressure) to achieve 60 g/m² grammage. For TOCNF-ECH Fe^{3+}, chemical crosslinking was first performed by adding 1 mL epichlorohydrin (ECH) and 5 mL hydrochloric acid (HCl) to the TOCNF suspension under stirring for 24 h. The chemically treated suspension was then processed identically to the TOCNF-Fe^{3+} method (filtration, $FeCl_3$ immersion, rinsing, and hot-pressing).

To provide a performance benchmark for these fabricated bio-based films, a polyethylene terephthalate (PET)-based commercial filter SFC-10 (METOLIGHT filter foil) was included in the study.[73]

In the **publication III**, CNCs were isolated from Norway spruce (*Picea abies*) pulp. The kraft pulp and oxygen delignified pulps are referred to in the subsequent text as unbleached softwood kraft pulp (UBSK) and bleached softwood kraft pulp (BSK), respectively. Kraft pulp was hydrolyzed using 58 or 64 wt% sulfuric acid (H_2SO_4) for 30 min at 55°C to obtain different CNC grades. Next suspensions were quenched in chilled water, dialyzed, and homogenized through a single pass at 1700 bar. Films (30 g/m^2) were cast from 0.4 wt% CNC suspensions and dried at 23°C and 50% RH.

In the **publication IV**, commercial CNCs (CelluForce) and CNF, homogenized at 1700 bar, were used. Films (25 g/m^2) were formed by solvent casting into polystyrene Petri dishes and dried at 23°C and 50% RH, followed by an additional drying step at 150°C for 1 h. Sodium montmorillonite clay (MTM) was added as a powder to the NC suspensions, with magnetic stirring overnight. Films were fabricated by mixing CNC and CNF suspensions at different mass ratios (75:25, 50:50, 25:75, 0:100) with and without MTM.

3.1.2 Dye solar cell fabrication and assembly

In the **publication II**, TiO_2-based DSSCs were fabricated using FTO substrates (Pilkington TEC-15, 15 Ohm/sq). Photoelectrodes were prepared by sequential doctor blading of transparent and active opaque TiO_2 nanoparticle layers, followed by heat treatment as described previously.[44] The photoelectrodes were sensitized with a Z907 Ruthenium Dye solution (0.3 mM) in a 1:1 mixture of acetonitrile and *tert*-butyl alcohol. Devices were assembled using an electrolyte that forms the I^-/I_3^- redox couple. This electrolyte contained 0.05 M I_2, 0.5 M 1-methylbenzimidazole (NMBI), 0.5 M 1-propyl-3-methylimidazolium iodide (PMII), and 0.1 M guanidinium thiocyanate (GuSCN) in 3-methoxypropionitrile (3MPN). The cells were sealed with a platinum-coated counter electrode, following protocols by Poskela et al.[44]

3.1.3 Perovskite solar cell fabrication and assembly

In the **publication VI**, four-pixel and eight-pixel PSCs were fabricated on both etched and unetched FTO substrates (TEC15). The four-pixel group ($20\times20\times2$ mm) substrates were partially etched using zinc (Zn) powder and 4 M HCl, while the eight-pixel group ($25.4\times25.4\times2.2$ mm) used pre-patterned FTO. For the four-pixel group, a compact TiO_2 (c-TiO_2) layer was deposited via spray pyrolysis using a 0.16 M Titanium diisopropoxide bis(acetylacetonate) ($Ti(acac)_2OiPr_2$) and 0.4 M acetylacetone precursor in ethanol at 460°C with an airbrush. Subsequently, a mesoporous TiO_2 (meso-TiO_2) layer was then spin-coated from a 150 mg/mL TiO_2 paste and sintered at 450°C. For the eight-pixel group, a c-TiO_2 layer was deposited by spray coating a 17.3 vol% solution in 2-propanol at 450°C over 12 layers, followed by annealing at 450°C for 45 min. The meso-TiO_2 layer was prepared similarly for the eight-pixel group.

A triple-cation mixed-halide perovskite $Cs_{0.05}(FA_{0.83}MA_{0.17})_{0.95}Pb(I_{0.83}Br_{0.17})_3$ (CsFAMA) was deposited via spin-coating. Annealing was performed at 100°C for 1 h inside a nitrogen-filled glovebox. For the four-pixel group, a 70 mM 2,2',7,7'-Tetrakis[N,N-di(4-methoxyphenyl)amino]-9,9'-spirobifluorene (Spiro-OMeTAD) solution in chlorobenzene was prepared and doped with 4-*tert*-butylpyridine (tBP), lithium bis(trifluoromethanesulfonyl)imide (LiTFSI), and Tris(2-(1H-pyrazol-1-yl)-4-*tert*-butylpyridine)cobalt(III) tris(bis(trifluoromethanesulfonyl)imide) (FK209) at molar equivalents of 3.3, 0.5, and 0.05, respectively. This doped solution was deposited onto the substrates via dynamic spin coating at 4000 rpm for 10 s. For the eight-pixel group, a 29.5 mM Spiro-OMeTAD solution in chlorobenzene was prepared with adjusted dopant concentrations, namely 3.2, 0.53, and 0.1 molar equivalents for tBP, LiTFSI, and FK209, respectively. An 80 μL aliquot of this

solution was dynamically spin coated at 1800 rpm for 30 s. Finally, gold electrodes (80–100 nm) were thermally evaporated as top contacts.

In the **publication VII**, carbon monolithic electrode (CME) (Solaronix) of the carbon electrode perovskite solar cells (C-PSCs) were infiltrated with methylammonium lead iodide ($MAPbI_3$) precursor solution (Solaronix) under nitrogen and heated at 50°C for 10 min.[74] Gold electrode perovskite solar cells (Au-PSCs) were fabricated following the procedure for the four-pixel group etched devices in the **publication VI**.

3.1.4 ZnO-based textile functionalization

In the **publication V**, cotton fabrics (140 g/m^2, 100%) were pre-cleaned in Decon90 solution (10 mL in 90 mL water) at 60°C for 15 min, dried at 50°C for 12 h, and immersed in 50 ml of 0.1 M sodium hydroxide (NaOH) for 10 min. A ZnO precursor solution was prepared by dissolving zinc acetate hydrate in ethanol at 60°C for 10 min under stirring, followed by the addition of ammonium hydroxide (NH_4OH) and NaOH or potassium hydroxide (KOH) (the total volume was 100 ml). The fabrics were immersed in the precursor solution and stirred at 300 rpm for 6 h at 30°C. The ZnO-coated fabrics were placed in a microwave oven at 800 W for 3, 4 or 5 min (depending on the sample). Samples were then rinsed with deionized water and dried at 50°C for 12 h.

3.1.5 3D-printed holder for PSC characterization

The holder used for the PSC characterizations in the **publication VI** and **publication VII** was three-dimensional (3D) printed with a Prusa MK3S+ 3D printer equipped with a 0.4 mm stainless steel nozzle. All prints were made inside the Original Prusa Enclosure to maintain consistent temperature, which ensured high-quality results. The prints used a satin powder-coated build plate and black EasyABS filament, chosen for its favorable mechanical and thermal properties. The print settings were adjusted to a layer height of 0.1 mm, yielding the necessary resolution for the 3D printed holder.

Harwin P70-1020045R spring-loaded “pogo” pins were inserted into the holder’s base to make electrical contact with the PSC electrodes. These pins were selected because their internal spring mechanism applies only minimal force to the cells. Copper wires were soldered to the rear side of the pins to connect to the measuring equipment. Neodymium magnets were installed at the corners of the holder lid to keep the PSC in position. The holder was designed so that the magnets exerted force primarily at the edges, thus without fully engaging the pogo pins.

Table 1. Summary of aging test parameters

Publications	ISOS protocol	Duration (h)	Cumulative radiant exposure at the 300–400 nm (MJ/m^2)
I, **II**	L-1	1000	240
III	L-1	500	1200
IV	L-1	1800	430
V	L-1	48	11
VII	D-1	9200	N/A

3.2 Characterization methods

3.2.1 Aging protocols

The accelerated aging tests, closely aligning with ISOS-L-1,[32] were conducted using an Atlas XLS+ solar simulator equipped with a xenon lamp (NXE 1700), simulating 1 Sun (air mass (AM)1.5G spectrum[42]). Environmental conditions during the experiment were controlled, with an ambient temperature of 35–36°C, a Black Standard Temperature (BST) of 60°C, and a relative humidity (RH) of 10–20%. A typical duration for the light soaking testing of PV is 1000 h under such conditions, which is equivalent to 1 year of outdoor exposure in Central Europe.[75] A Fluke TiS75 thermal imaging camera was used to monitor the sample temperatures, which were typically around 45°C, while ambient temperature was 22°C. The simulator was equipped with cooling fans to regulate the lamp temperature, generating a strong airflow. To ensure sample stability, custom-built sample holders were designed for each study.

In contrast, unencapsulated PSCs in **publication VII** were aged under ISOS-D-1 conditions (dark storage).[32] The temperature (22 ± 1°C) and RH (40 ± 20%) were continuously monitored using a RuuviTag Bluetooth sensor.[76] The aging durations varied by study, as detailed in Table 1.

3.2.2 UV-Vis-NIR spectroscopy

In the publications **I**–**V** optical properties of the materials were evaluated using UV-Vis-NIR spectroscopy. The key differences of the UV-Vis-NIR measurement setups used across the five studies are summarized Table 2. Usual light source change wavelength was around 300–350 nm.

3.2.3 Solar cell current-voltage characterization

The electrical performance of solar cells studied in the **publication II**, **publication VI**, and **publication VII** was periodically assessed through IV (or current density-voltage (JV)) measurements. To achieve reliable and reproducible measurement re-

Table 2. UV-Vis-NIR methods for different publications.

Publications	Measuring equipment	Range (nm)	Light source(s)
I, **IV**	Agilent Cary 5000 (Diffuse Reflectance Accessory)	200–800	Deuterium (UV) & Tungsten-Halogen (Vis)
II	Shimadzu UV-2600 + ISR-2600 Plus Sphere	200–1100	Deuterium (UV) & Halogen (Vis-NIR)
III	PerkinElmer PDA UV/Vis Lambda 265	200–800	Deuterium (UV) & Tungsten-Halogen (Vis)
V	UV–Vis Specord 200 Plus	200–700	Deuterium (UV) & Halogen (Vis)

Table 3. Summary of IV measurement parameters

Publication	Solar cell type	Measuring equipment	Solar simulator	Scan rate (mV/s)	Mask aperture (mm^2)
II	DSSC	PalmSens4	Peccell PEC-L01	20	80
VI	Four-Pixel PSC	Keithley 2636	Newport Oriel 92250A	50	12
	Eight-Pixel PSC	Keithley 2450	Wavelabs Sinus-70	50	10
VII	C-PSC	PalmSens4	Peccell PEC-L01	100	64
	Au-PSC	PalmSens4	Peccell PEC-L01	100	13

sults by alleviating alignment issues and minimize the relative influence of edge effects such as stray light, the photomasking with device-specific aperture sizes was used.[77] The key differences of the IV measurements between all three studies are summarized in Table 3.

In the **publication II** and **publication VII**, a PalmSens4 potentiostat was used in combination with a Peccell PEC-L01 class A solar simulator, equipped with a short-arc xenon lamp designed to simulate 1 Sun AM1.5G spectrum. This solar simulator provided 1000 W/m^2 illumination, and a single IV scan was conducted in both forward and reverse directions (sweeps) after a 3-second stabilization period. IV data was analyzed and plotted using a Python (3.9) script.[78]

In the **publication II**, DSSCs were maintained at ambient temperature and masked with black electrical tape featuring an 80 mm^2 rectangular aperture. The voltage was swept from -0.2 V to 0.85 V and back to -0.2 V, with increments of 10 mV and a scan rate of 20 mV/s.

In the **publication VI**, IV measurements were performed on two groups of PSCs with varying pixel counts, each tested under different setups:

- **Four-pixel group**: Characterized using a Newport Oriel Instruments model 92 250A solar simulator and a Keithley 2636 source measure unit (SMU) under 1 Sun illumination (100 mW/cm^2 AM1.5G). A 50 mV/s scan rate was applied in both forward and reverse directions.

- **Eight-pixel group**: Measured using a Wavelabs Sinus-70 solar simulator and a Keithley 2450 SMU under 1 Sun illumination. The scan rate remained the same as for the four-pixel group.

In the **publication VII**, IV measurements were conducted for both C-PSC and Au-PSC. The scan conditions were similar, except:

- C-PSC: Voltage ranged from -0.2 V to 1.0 V, with increments of 10 mV and a scan rate of 100 mV/s. A 3D-printed sample holder with an integrated aperture mask was used.

- Au-PSC: The scan range extended from -0.2 V to 1.2 V in both directions.

3.2.4 Digital image acquisition

Standardized image acquisition were employed to ensure reproducibility and accuracy across publications **I**-**V**, and **VII**. Digital photographs were captured inside a custom-build photography chamber with neutral gray interior walls to minimize reflections and color biases. A Sony A7 MK2 camera coupled with a Laowa 100 mm f/2.8 macro 2×lens was utilized with uniform LED illumination (LED Neon Flex N-6×12-z-11 W-40 k-01, 4000 K color temperature, and a luminous flux of 1150 lm). Consistent camera settings (ISO 200, aperture f/11, shutter speed 1/20 s) and manual focus were maintained. At the beginning of each photo session an image of an X-Rite ColorChecker Passport was taken to utilize it as a baseline for white balance and minor exposure correction.

All images were captured in RAW format (.ARW), post-processed in Adobe Photoshop Lightroom Classic (10.3 Release), and exported as JPEG files (opRGB). The post-processing steps included:

- digital negative (DNG) color profile: applying a camera and lens specific color profile based on the X-Rite ColorChecker Passport

- white balance: applied based on a third neutral gray step rectangle of the X-Rite ColorChecker Passport

- exposure compensation (optional): done based on the image of the X-Rite ColorChecker Passport to ensure its digital appearance to be consisted between different photo sessions and then synchronized with images of the samples

- cropping (optional): reducing the size of the image to the area of interest

All RGB values reported herein were obtained from images captured and processed explicitly within the opRGB.[64,65] For brevity, opRGB will henceforth be referred to simply as RGB unless otherwise stated.

3.3 Analysis and modeling

3.3.1 Color analysis

Color analysis was performed by extracting RGB values from multiple distinct non-reflecting areas of each sample image (see Subsection 3.2.4). Average RGB values were analyzed using custom scripts in Python (3.9)[79] (**publication I**, **publication V**, **publication IV**, **publication VII**) or MATLAB (version R2021a, **publication III**). The RGB values were further transformed into the perceptually uniform CIELAB (**publication I**, **publication VII**) to quantify human-perceivable color changes effectively. Color alteration was quantified and analyzed using various approaches described below.

- For the **publication I**, NC-based films color changes between initial and final images were quantified through Euclidean distance in the RGB space (ΔRGB), calculated using an Equation (1):

$$\Delta RGB = \sqrt{(R_{\text{Initial}} - R_{\text{Final}})^2 + (G_{\text{Initial}} - G_{\text{Final}})^2 + (B_{\text{Initial}} - B_{\text{Final}})^2} \tag{1}$$

  The uniformity of the color changes across multiple selected areas was assessed by calculating the standard deviation of color change vectors ($\sigma_{\Delta RGB}$) from different regions (Equation (2)):

$$\sigma_{\Delta RGB} = \sqrt{\frac{1}{n-1}\sum_{i=1}^{n}(\Delta RGB_i - \overline{\Delta RGB})^2} \tag{2}$$

  where n is the number of areas per image, D_{RGB_i} is the ΔRGB for the *i*-th area, and $\overline{\Delta RGB}$ is the mean of ΔRGB across all areas.

  Changes in perceived lightness (ΔL^*) were evaluated using an Equation (3):

$$\Delta L^* = L^*_{\text{final}} - L^*_{\text{initial}} \tag{3}$$

  The standard deviation of ΔL^* cross multiple areas was calculated similarly to the Equation (2).

- In the **publication II**, the overall color intensity change of the NC-based films and electrolyte of DSSCs was analyzed using the square root of the square root of the sum of squares (SRSS) of RGB coordinates an Equation (4):

$$\text{SRSS}_n = \sqrt{R_n^2 + G_n^2 + B_n^2} \tag{4}$$

  where R_n, G_n, and B_n represent the R, G, and B color coordinates, respectively, for the *n*-th measurement. These values were normalized relative to the initial measurement to track changes over time.

- In the **publication V**, digital images were recorded periodically (see Subsection 3.2.4) for stained areas (methylene blue (MB) and coffee) and corresponding unstained areas on the same fabric samples, to simultaneously account for UV-driven degradation or discoloration of the cotton material substrate. The stain removal efficiency was quantified by calculating the ΔRGB (Equation (1)) between the stained and unstained regions at each specific time point for each sample. Therefore, the obtained ΔRGB at each time point directly quantifies how much the stained area color deviates from the simultaneously measured background color, effectively correcting for fabric discoloration or degradation. The stain removal efficiency at a given time was expressed as a percentage reduction of the ΔRGB, relative to the initial distance between the stained and unstained areas before irradiation began.

  The stain removal efficiency (%) was determined by comparing the ΔRGB relative to the color difference at the previous time point ΔRGB_{n-1} (Equation (5)):

$$\text{Efficiency (\%)} = \frac{\Delta RGB_{n-1} - \Delta RGB_n}{\Delta RGB_{n-1}} \times 100\% \tag{5}$$

  Higher positive values indicate greater stain removal efficiency at the current interval, while negative values would suggest increased staining or color darkening compared to the previous measurement. This methodology accounts for simultaneous background degradation, as the unstained background region serves as an internal reference, reducing potential errors arising from fabric degradation effects.

- In the **publication VII** the ΔE_{DIN99} [61] was used to assess quantitatively visual changes in the PSCs over time. In addition, Pearson correlation analysis was used to quantify the linear relationship between the measured color changes and the degradation in electrical performance, yielding a correlation coefficient (*r*) and a significance value (*p*). [80]

A consistent methodology preceded by the UV-induced aging protocol (see Subsection 3.2.1) schematically presented as a flowchart in Figure 2. Despite the specific aging protocol presented, this flowchart can be applied to any color change study with or without aging involved.

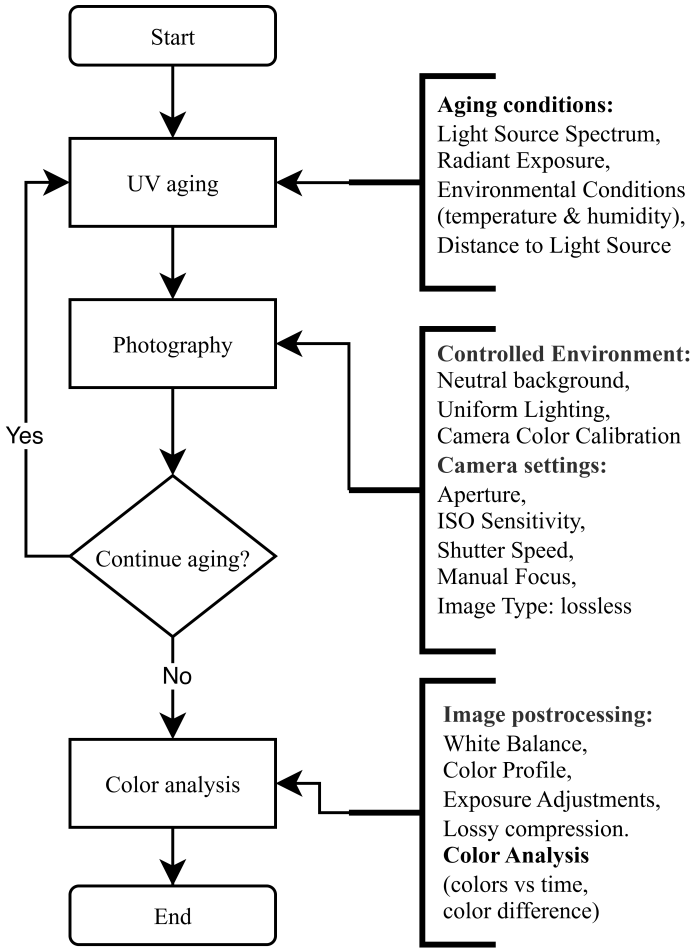

Figure 2. Flowchart of image acquisition and analysis protocol applied across publications, highlighting essential parameters and processing steps. Adapted from the **publication V** under a CC BY 4.0 license.

3.3.2 Predictive modeling

Predictive modeling[44] was used to evaluate long-term performance trends in DSSCs by analyzing electrolyte color changes and estimating the limiting current (I_{lim}). The electrolyte color was assessed by converting the B channel of RGB into the Y component in the cyan, magenta, and yellow color space (CMY) color space us-

ing Equation (6):

$$Y = 255 - B \tag{6}$$

This transformation provides an indirect measure of electrolyte degradation, which correlates with the limiting current I_{lim}—the maximum current a DSSC can transfer. I_{lim} was calculated as Equation (7):

$$I_{\mathrm{lim}} = \frac{4FD_{I_3^-}c_{I_3^-}}{d} \tag{7}$$

where F is the Faraday constant, $D_{I_3^-}$ is the diffusion coefficient of tri-iodide, $c_{I_3^-}$ is the concentration of tri-iodide, and d is the electrode separation distance. As the DSSC undergoes degradation, the concentration of $\mathrm{I_3^-}$ declines, leading to a corresponding reduction in I_{lim}. To predict long-term behavior, the model estimates the rate of $\mathrm{I_3^-}$ concentration loss by analyzing the bleaching rate of the electrolyte.

The only empirical input required for model fitting is the initial short-circuit current density (J_{SC}), taken as the maximum J_{SC} during the prediction period. To ensure clear visualization of the initial conditions, J_{SC} values were adjusted by an arbitrary factor of 1.1 to account for potential early-stage stabilization effects. Uncertainty in J_{SC} was considered by defining a range of ±20% around the maximum J_{SC} value. This approach distinguishes the empirical data from the model's predictions, facilitating the estimation of DSSC degradation trends over time.

3.3.3 Ultraviolet protection factor

In the **publication V**, UV protection factor of ZnO-coated cotton fabrics using the ultraviolet protection factor (UPF).[81,82] UPF is defined as the ratio of average effective UV irradiance (290–400 nm) without and with the fabric, calculated using Equation (8):

$$UPF = \frac{\sum_{\lambda=290}^{\lambda=400} E(\lambda)\, S(\lambda)\, \Delta\lambda}{\sum_{\lambda=290}^{\lambda=400} E(\lambda)\, S(\lambda)\, T(\lambda)\, \Delta\lambda}. \tag{8}$$

Here, $E(\lambda)$ is the erythema action spectrum, $S(\lambda)$ is the solar spectral irradiance, $T(\lambda)$ is the fabric transmittance at wavelength $\Delta\lambda$, and $\Delta\lambda$=5 nm in this work. Textiles with UPF>15 are classified as UV-blocking and those with UPF>40 as providing "excellent protection".

4 Results and Discussion

4.1 Composition of NC-based films impacting long-term UV stability

4.1.1 **Publication I**: Lignin-enhanced NC films

Building on earlier demonstrations of color-based degradation assessment,[44] the **publication I** investigates NC-based films (Subsection 3.1.1). Key aspects evaluated were the films' UV-shielding stability, their visual appearance, and their spectroscopic properties over the 1000-hour light exposure period (Subsection 3.2.1). Since neat CNF and TOCNF lack inherent UV protection required for photovoltaic applications (when used as UV filters), lignin was incorporated to grant UV-shielding capabilities. Visual inspection and color alteration analysis revealed minimal changes in film appearance (Subsections 3.2.4 and 3.3.1). Films containing lignin — either as residual lignin in the fiber or as added lignin nanoparticles — exhibited remarkable UV-shielding ability that they maintained throughout the test (<1% transmittance below 390 nm), whereas neat NC remained UV-transparent (Subsection 3.2.2). To further validate the UV-blocking efficacy, NC films were placed on top of polyvinyl chloride (PVC) substrates during the exposure. Although minor degradation of the lignin-containing films occurred, they continued to provided full UV protection, thereby preventing discoloration of the underlying PVC substrates. Overall, lignin-modified NC films demonstrated excellent long-term visual stability and robust UV-blocking performance, highlighting their potential for use in sustainable optoelectronic applications.

To track and assess photostability of NC-based films, digital images were recorded during the 1000 h of artificial sunlight exposure (Figure 3). Visual inspection of these images revealed distinct characteristics of each film's composition. The neat CNF and TOCNF films appeared translucent with white nuances at the beginning, while the lignin-containing samples (Ligno-CNF, Ligno-TOCNF, CNF with lignin nanoparticles (produced according to the **publication I**) (CNF-LNP), and TOCNF-LNP) exhibited brownish shades typical of lignin-rich materials.[83] Minimal color changes were observed after 1000 h of exposure, with the most pronounced color alterations occurring during the first 50 h (Figure 4).

Quantitative analysis of color alterations followed similar trends (Figure 4 and Table 4). Neat CNF showed only moderate changes in its RGB channels—the small

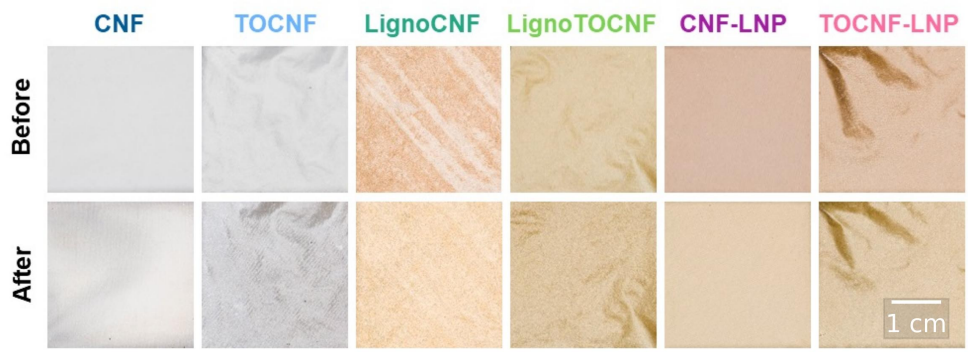

Figure 3. Photographic overview of six lignin-containing and lignin-free NC-based films before and after 1000 h of artificial sunlight exposure. The top row shows the initial state, revealing translucent white nuances in the neat cellulose films and brownish hues in lignin-containing ones. The bottom row illustrates the same films following the exposure period. The photos suggest that the visual appearance of all NC films remained largely unchanged after light exposure. Adapted from the **publication I** under a CC BY 4.0 license.

overall color shift is reflected in relatively low ΔRGB and ΔL^* values. Low color changes occurred alongside high variability across areas revealed local surface heterogeneity. Conversely, TOCNF darkened noticeably, evidenced by a pronounced drop in its RGB and further supported by its high ΔRGB and negative ΔL^*. Lignin-containing films (Ligno-CNF, CNF-LNP, and TOCNF-LNP) exhibited slight brightening. This photobleaching can be explained by lignin's phenolic groups forming radicals, which degrade into less colored aliphatic acids.[84] By contrast, Ligno-TOCNF darkened (negative ΔL^*), suggesting the formation of new chromophores through photo-oxidation.[22]

Table 4. Quantitative color alteration metrics (ΔRGB and ΔL^*) in NC-based films after 1000 h of artificial sunlight. The ΔRGB value represents the Euclidean distance in RGB between initial and final states, while ΔL^* indicates the difference in perceived lightness (positive for brightening, negative for darkening) in CIELAB. Adapted from the **publication I** under a CC BY 4.0 license.

	CNF	TOCNF	Ligno-CNF	Ligno-TOCNF	CNF-LNP	TOCNF-LNP
ΔRGB	6 ± 6	35 ± 7	23 ± 5	17 ± 4	26.9 ± 0.8	13 ± 4
ΔL^*	0.6 ± 1.1	-3.5 ± 0.8	2.7 ± 0.5	-1.3 ± 0.2	3.3 ± 0.2	1.6 ± 0.4

To investigate how color alterations can be tied to changes in the optical behavior of the films, UV-Vis-NIR spectroscopy was performed (Figure 5). Neat cellulose films (CNF and TOCNF) showed the highest transmittance (approximately 80% in the visible region), with UV absorption becoming significant below 300 nm (Figure 5a). Despite their seemingly stable color appearance (Figure 3), both films displayed a decrease in transmittance following the aging test, especially for wave-

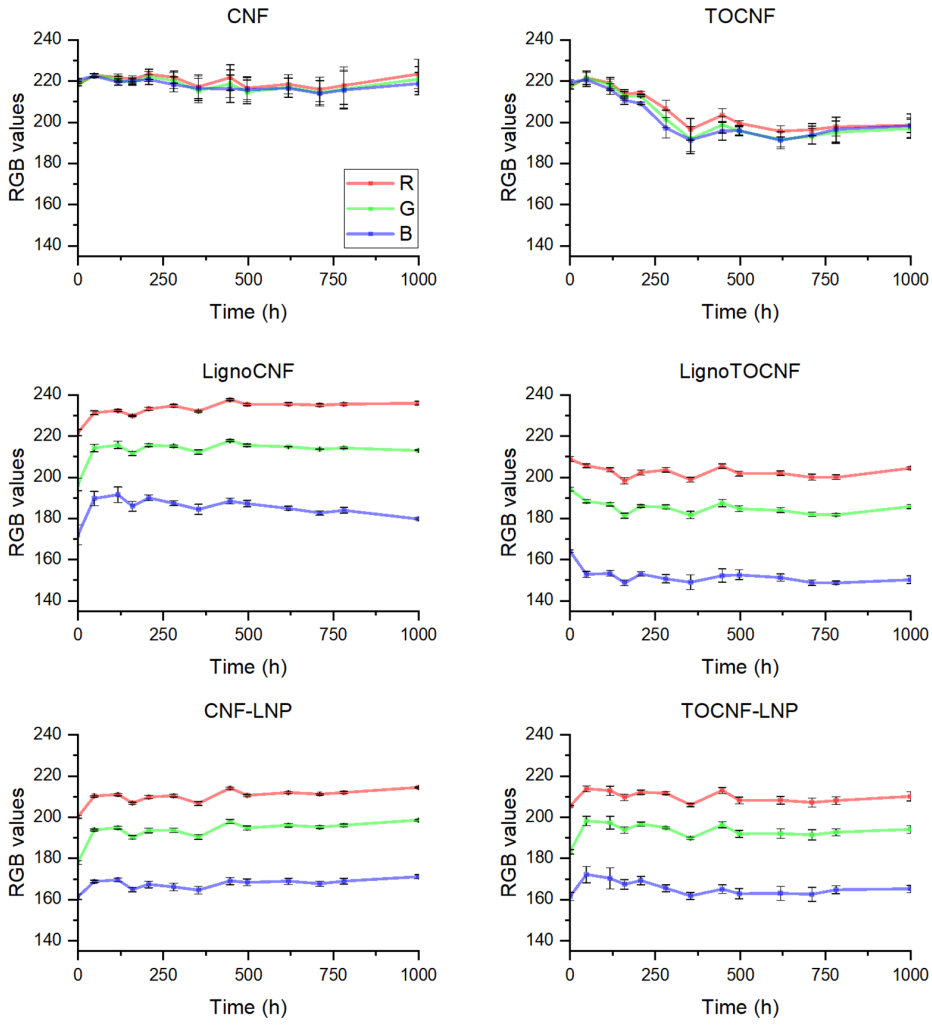

Figure 4. R, G, and B evolution of NC films over 1000 h of 1 Sun solar exposure. Each panel corresponds to one of the six NC-based films from Figure 3. R, G, and B values were extracted from digital images in three different film regions and averaged to generate representative color coordinates. The error bars show the standard deviation among these regions. Adapted from the **publication I** under a CC BY 4.0 license.

lengths under 600 nm. All NC films exhibited some light scattering, as evidenced by noticeable haze (Figure 5b).

The UV-screening effect in the lignin-containing films is fundamentally based on the phenolic and aromatic nature of the lignin molecule. Lignin contains a variety of chromophoric groups—including aromatic rings, carbonyls, and conjugated double bonds—that are highly effective at absorbing UV radiation.[16] These same chemical structures are also responsible for absorbing some light in the visible spectrum, which results in the films' reduced transparency and brownish color.[16] This mechanism explains why these films demonstrated high UV shielding up to around 400 nm, though sacrificing transparency in the visible range (Figure 5a). After aging, Ligno-CNF, CNF-LNP, and TOCNF-LNP each showed approximately a 10% increase in transmittance, which is consistent with photobleaching. Interestingly, the Ligno-TOCNF sample was the only one that exhibited a decrease in transmittance upon exposure, matching its earlier color changes (Figure 4). Nonetheless, the strong UV shielding provided by lignin may justify the loss of visible transparency in application where fully biodegradable films are required.

To practically test the films' UV-blocking performance, samples were placed on top of rigid PVC substrates. Given that PVC undergoes chemical and physical changes under UV exposure,[85] substrate discoloration served as a visual indicator of the corresponding NC films' UV shielding effectiveness (Figure 6). PVC beneath lignin-enhanced films exhibited minimal color changes, indicating effective UV protection. In contrast, significant discoloration was observed under neat cellulose films (CNF, TOCNF), corresponding to poorer UV protection capabilities. Quantitative color analysis confirmed these visual observations, showing significantly higher discoloration for samples under neat cellulose films compared to lignin-containing films (Table 5). The surface inhomogeneity of the CNF film is responsible for its irregular UV shielding, which is visually evident as unequal discoloration of the PVC substrate (Figure 6). This explanation is strongly supported by the high standard deviation observed in the film's own RGB value changes over time (Figure 4).

Table 5. Quantitative color changes in PVC samples underneath the NC films after 1000 h of solar aging. The same color-difference parameters (ΔRGB and ΔL^*) as in Table 4 are presented. Adapted from the **publication I** SI under a CC BY 4.0 license.

	CNF	TOCNF	Ligno-CNF	Ligno-TOCNF	CNF-LNP	TOCNF-LNP
ΔRGB	64 ± 24	81 ± 7	9 ± 8	9 ± 5	12 ± 7	12 ± 8
ΔL^*	-7 ± 2.9	-9.5 ± 1.8	-1.1 ± 1.2	-1.1 ± 0.9	-1.4 ± 0.8	-1.4 ± 1.1

These results show consistent agreement between the colorimetric data, UV-Vis-NIR spectra, and PVC discoloration tests. The following section investigates other bio-based UV absorbers in NC films.

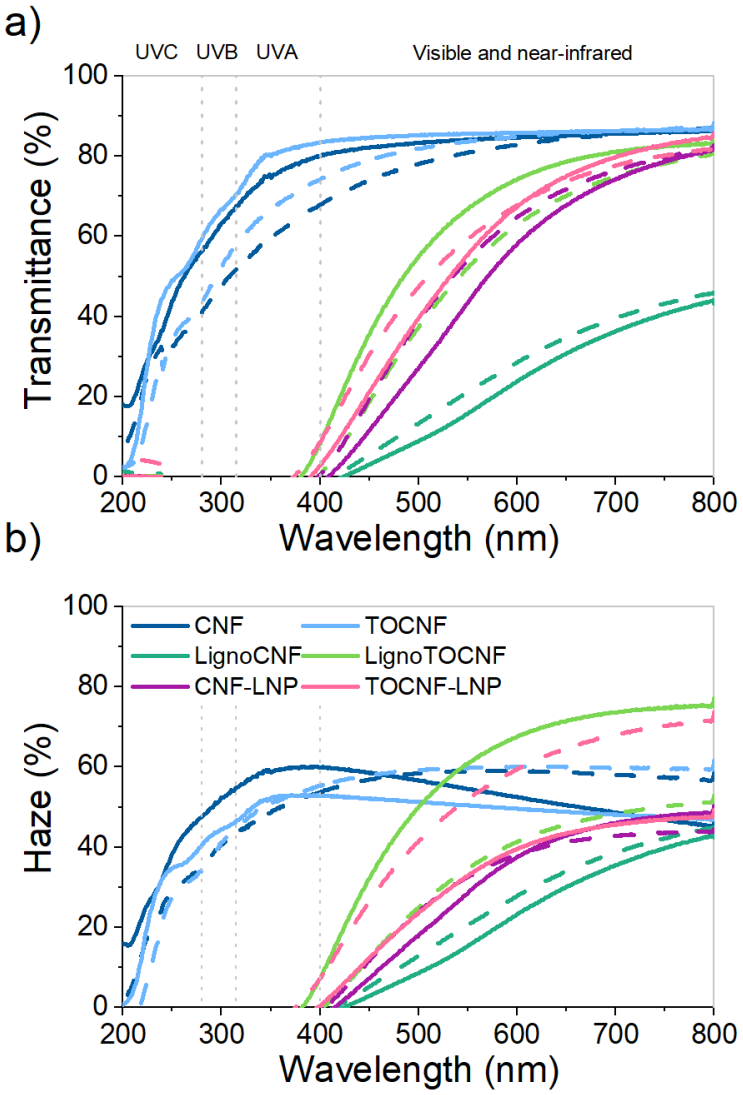

Figure 5. Transmittance and haze spectra for NC films, before (solid line) and after (dashed line) 1000 h of artificial sunlight. **(a)** Transmittance curves recorded over 200–800 nm demonstrate that neat CNF and TOCNF provide high transparency in the visible region (up to 80%) and lack of UV absorption. **(b)** Haze measurements reveal scattering-related shifts possibly linked to morphological reorganizations or moisture release. Both panels copare to original publication are now featuring doted lines indicating different spectral reagions, namely UVC, UVB, UVA, and visible/near-infrared regions. Adapted from the **publication I** under a CC BY 4.0 license.

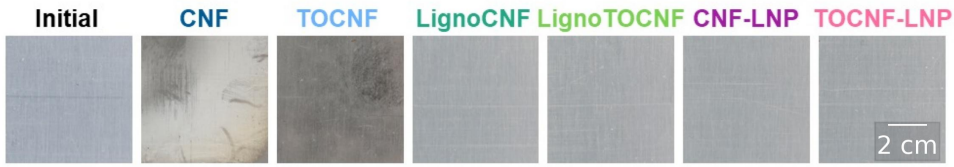

Figure 6. Discoloration of underlying PVC samples covered by NC films after 1000 h of simulated sunlight. Each panel features a PVC piece protected by one of the six NC-based samples, and a reference intial state one. Adapted from the **publication I** under a CC BY 4.0 license.

4.1.2 **Publication II**: Bio-based UV filters for photovoltaics

Where the **publication I** focused on lignin's UV-shielding effect, the **publication II** further adapts the color-based assessment method to examine the long-term stability of four different bio-based UV filters (Subsection 3.1.1). Similar to the **publication I**, these films were subjected to accelerated aging tests under artificial sunlight for 1000 h (Subsection 3.2.1), with their optical performance and visual stability assessed through UV-Vis-NIR spectroscopy and color alteration analysis (Subsections 3.2.2 and 3.3.1). This work specifically examines the films' performance in protecting DSSCs—devices that are extremely prone to UV-induced degradation[44] (Subsection 3.1.2). In the visible range, the CNF film dyed with red onion (*Allium cepa*) dye (CNF-ROE) film outperformed the other bio-based filter films, although not the conventional PET-based SFC-10 filter. In the UV range, however, CNF-ROE exhibited exceptional UV-blocking capabilities, reducing transmittance below 400 nm by over 99.9 %, surpassing even the commercial filter. These findings highlight the strong potential of bio-based filters for sustainable optoelectronic applications.

To evaluate the effectiveness and photostability of bio-based filter films, the digital imaging method (Subsection 3.2.4) were used over 1000 h of artificial sunlight exposure. A visual analysis, similar to that conducted in the **publication I**, of UV-filter films revealed distinct initial appearances corresponding to their compositions (Figure 7). These included nearly transparent SFC-10, reddish CNF-ROE,[26,86] brownish GDE coated CNF film with colloidal lignin particles deposition (produced according to the **publication II**) (CNF-LNP),[69] and lightly brownish iron-containing TOCNF-based films.[70,71] Within the first 24 h, significant discoloration was observed in iron-containing filters (TEMPO-mediated oxidized CNF film with physically crosslinked iron ions (III) (TOCNF-Fe^{3+}), TEMPO-mediated oxidized CNF film with epichlorohydrin induced chemically-physically crosslinked iron ion (III) (TOCNF-ECH Fe^{3+})), indicating rapid photodegradation that continued further. SFC-10 and CNF-ROE demonstrated remarkable visual stability throughout the test, whereas CNF-LNP exhibited moderate discoloration (Figure 7). Interestingly, a sim-

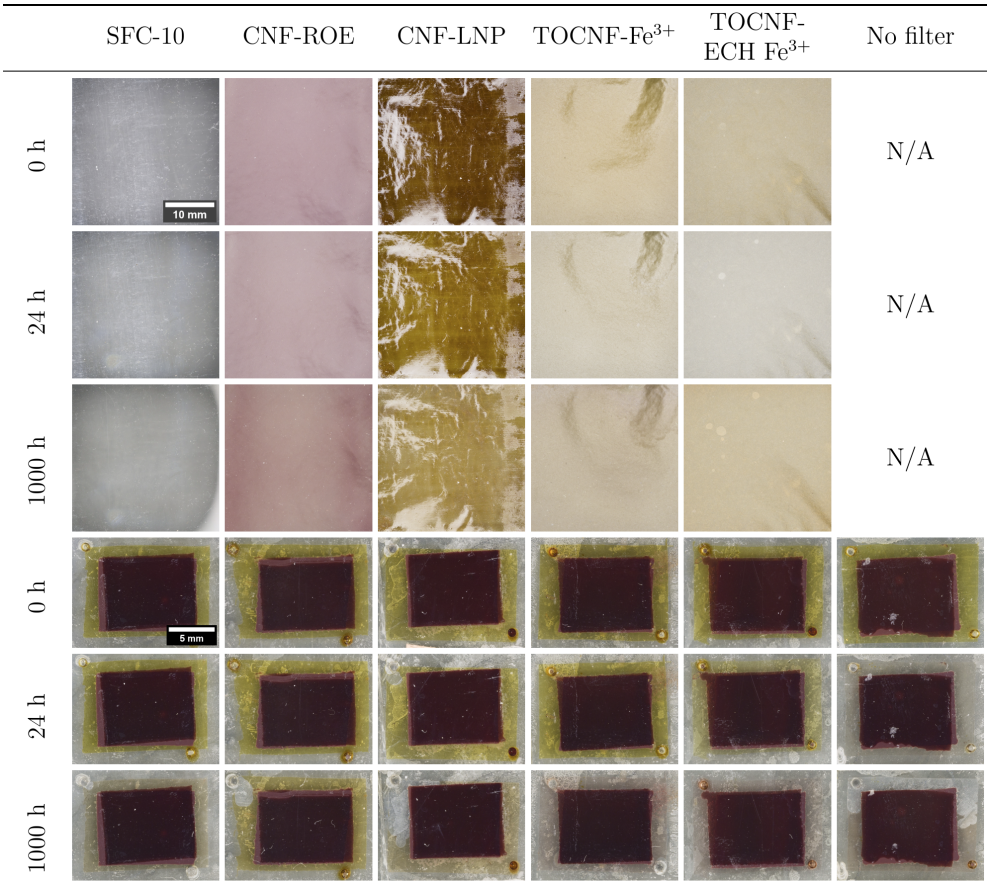

Figure 7. Visual assessment of UV-filter films (top) and corresponding underlying DSSCs (bottom) over 1000 h of artificial sunlight exposure. Focus on the yellow hue of the DSSCs' electrolyte, indicating the degradation of the redox couple over time, which directly affects the solar cell's performance. Adapted from the **publication II** under a CC BY 4.0 license.

ilarly rapid color shift was shown in the **publication I**, although in different film compositions.

Quantitative color analysis using normalized SRSS values of RGB channels (Figure 8a) further emphasized color shift observations. A normalization to the initial measurement was used to reduce the complexity of monitoring three components of RGB and unifying them into a single variable. The CNF-LNP filter film experienced significant initial color intensity change, indicative of surface modifications likely caused by epoxy degradation, followed by relative stabilization. The remaining films, particularly CNF-ROE and SFC-10, exhibited stable color profiles throughout exposure (Figure 8a). Remarkably, a distinct color shift was observed at the 24-hour mark, especially for TOCNF-ECH Fe^{3+}, consistent with the results in Figure 7.

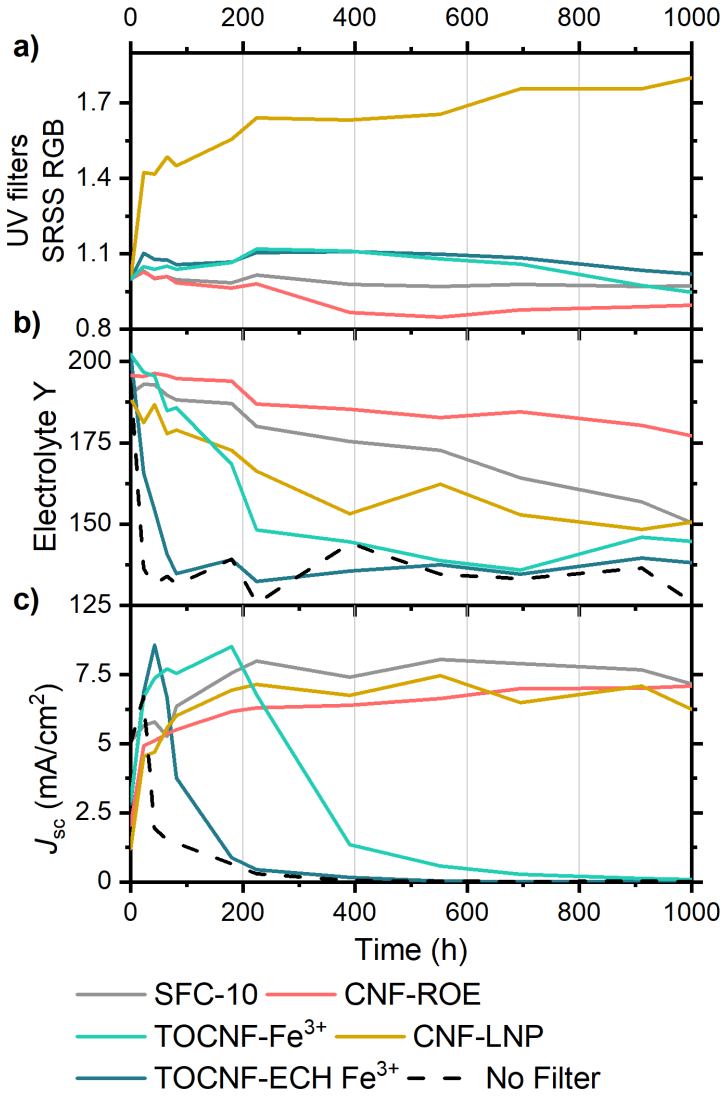

Figure 8. Comparative quantitative evaluation of various UV filter films, and the DSSCs devices they protect during artificial sunlight exposure. **(a)** Time-dependent normalized change in the SRSS of mean RGB values for the UV filter films. **(b)** Evolution of the Y color coordinate in the electrolyte of DSSC shielded by different UV filters. **(b)** Progression of J_{SC} over time for each DSSC category. All subfigures use a unified legend denoting the respective UV filter film types. Adapted from the **publication II** under a CC BY 4.0 license.

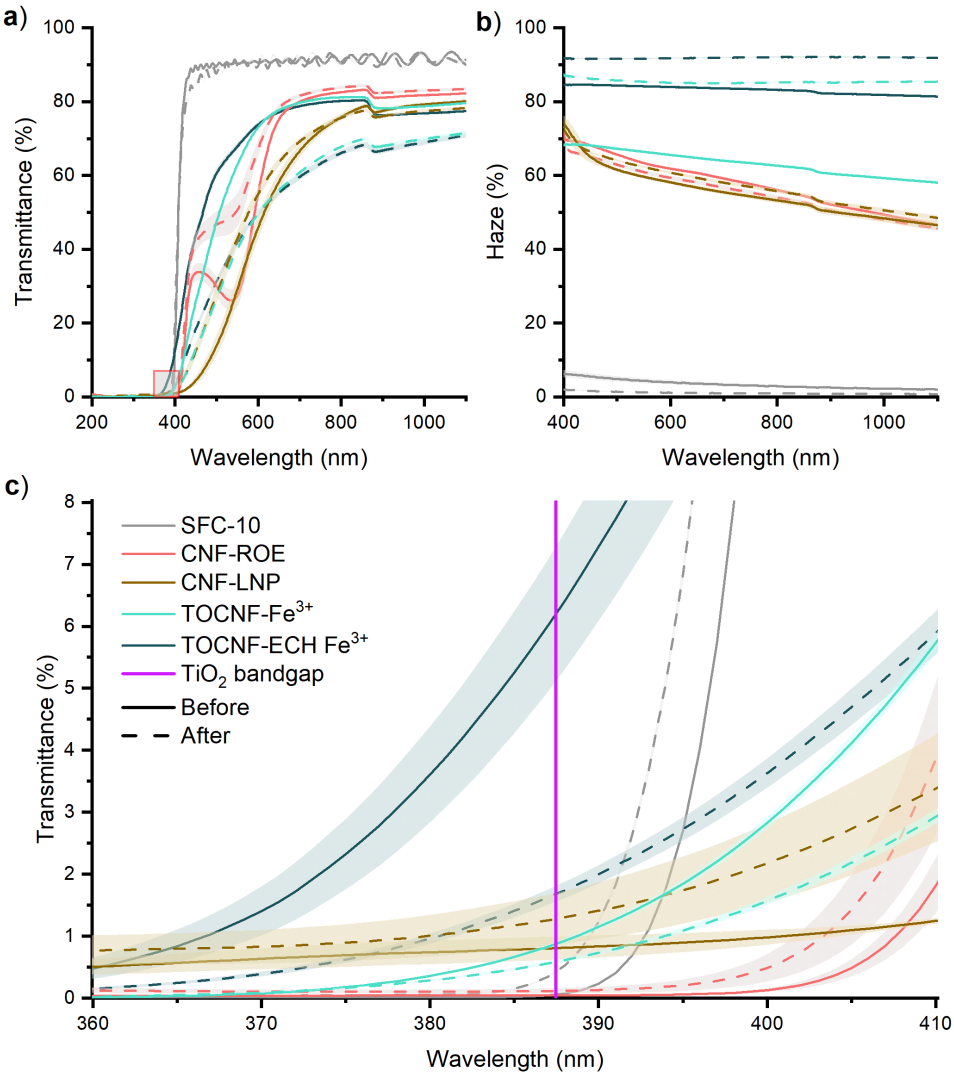

Figure 9. UV-Vis-NIR spectroscopy of the UV-filter films before (solid lines) and after (dashed lines) 1000 h of artificial sunlight aging: **(a)** transmittance over 200–1100 nm, **(b)** haze profile from 400–1100 nm (due to noise below 400 nm), **(c)** magnified transmittance from 360–410 nm centered at the TiO_2 band gap (vertical magenta line). Shaded areas represent standard deviation across three measured regions on each film. The panel **(c)** is enlarged compared to its original publication to improve the readability and distinguishability of the closely-spaced spectral lines. Together, these data highlight significant differences in the durability and light-management properties of bio-based UV-filter films under long-term stress. Adapted from the **publication II** under a CC BY 4.0 license.

To evaluate the UV-shielding efficacy of the films, their optical spectra were measured both before and after 1000 h of accelerated aging. Figure 9 displays the UV-Vis-NIR results, including (a) transmittance, (b) haze, and (c) a close-up of the spectra around the TiO_2 band gap ($\sim$ 387.5 nm).[87] The commercial reference, SFC-10 (gray lines), offered excellent initial UV-blocking (nearly 100% up to $\sim$390 nm) with high visible-range transmittance and very low haze (Figure 9a and b), maintaining these characteristics almost unchanged throughout the exposure. Nevertheless, even minor changes around the TiO_2 band gap can significantly impact sensitive applications such as DSSCs, where small increases in transmitted UV radiation can lead to a severe electrolyte degradation.[42] For instance, despite initially blocking 99.9% of radiation below 390 nm, after aging, SFC-10 shifted its cutoff wavelength to approximately 385 nm, allowing potentially harmful radiation to reach the solar cell (Figure 9c).

Turning to the bio-based films, CNF-LNP (brown lines) initially showed modest UV absorption below 390 nm but only about 40% visible transmittance at 600 nm. Interestingly, its transmittance in the visible region increased by roughly 10% following aging, although UV blocking near 390 nm weakened slightly (from about 0.6% to 1.2% transmittance between 200 and 390 nm) (Figure 9c). The iron-cross-linked films, TOCNF-Fe^{3+} (cyan) and TOCNF-ECH Fe^{3+} (dark teal), both started with relatively high visible-range transmittance ($\sim$80% at 600 nm) and effectively blocked over 98% of light below $\sim$380–390 nm (Figure 9c). Nonetheless, they each suffered a $\sim$20% decline in visible transmittance during the 1000 h test, and a rise in haze of 10–20% (Figure 9a and b). These optical changes imply partial breakdown or structural rearrangement within the iron-cross-linked matrix. However, despite the visible-range degradation, both films retained sufficient UV-shielding capability to prevent severe UV-induced damage.

Finally, the CNF-ROE film (red lines) stood out due to its excellent overall performance. It maintained a consistent UV cutoff near 390 nm and preserved more than 80% transmittance at 600 nm throughout the aging test (Figure 9c). Only a minimal shift occurred near the TiO_2 band edge, attributable to the robust anthocyanin-based UV absorption in the red onion extract. Moreover, comparisons at 390 nm revealed that CNF-ROE effectively matched or even surpassed SFC-10 in blocking UV. This remarkable combination of effective UV-filtering and consistent transparency within the visible spectrum makes CNF-ROE one of the most promising bio-based UV filters for optoelectronic applications.

4.1.3 **Publication III**: Isolation of mixed cellulose composition

Following up on earlier results with NC film findings, the **publication III** investigates different CNF suspensions with varying qualities. The study explored how different acid hydrolysis conditions—H_2SO_4 concentration of 58 or 64 wt% and

pulp type (bleached or unbleached)—influence crystalline lignocellulose isolates and their films (Subsection 3.1.1). The milder 58 wt% hydrolysis yielded dimension-spanning suspensions with higher yield and increased viscosity LNP formation in UBSK-derived samples was identified, enabling UV absorption and photostability. These findings demonstrate how tuning hydrolysis parameters tailors crystallinity, morphology, and stability for diverse NC applications.

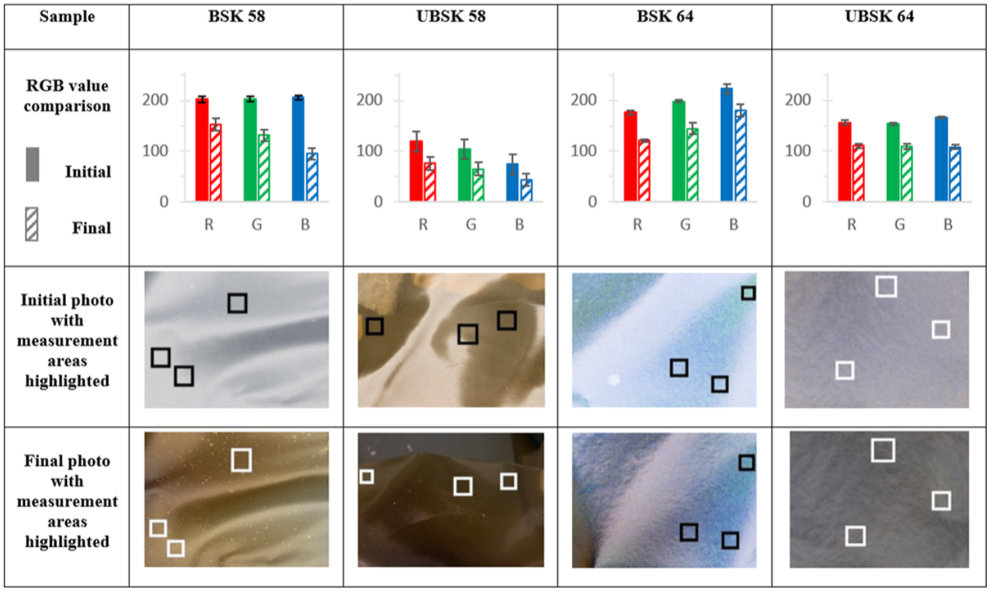

Figure 10. Comparative RGB data and photographs of CNC films before and after exposure. Each column corresponds to a specific hydrolysis route (BSK 58, UBSK 58, BSK 64, UBSK 64), with bar graphs in the top row displaying initial (solid) and final (hatched) R, G, and B values, averaged from multiple measurement areas. The middle and bottom rows show representative images of each film surface before and after 1000 h of simulated solar aging, with black/white squares outlining the same approximate regions used for color extraction. Error bars on the bar plots indicate the standard deviation among measurement areas. Adapted from the **publication III** under a CC BY 4.0 license.

To assess the long-term photostability of the CNC films, their discoloration was monitored under continuous simulated solar exposure (Subsections 3.2.1 and 3.2.4). Visual (Figure 10) and quantitative analysis (Figure 11) revealed that all the films darkened over exposure, indicating UV-induced degradation. However, the degradation behavior varied considerably depending on the films' acid hydrolysis conditions and chemical composition. The BSK 58 film underwent notable color shifts from neutral gray to distinct yellow hues around 150 hours of sunlight exposure (Figure 11a). The films treated with harsher acid conditions (BSK 64 and UBSK 64) showed rapid initial discoloration within 150 hours, which stabilized thereafter (Figure 11b and d). This greater photostability can be attributed to lower hemicellulose or the presence of residual lignin. This result is also in agreement with the litera-

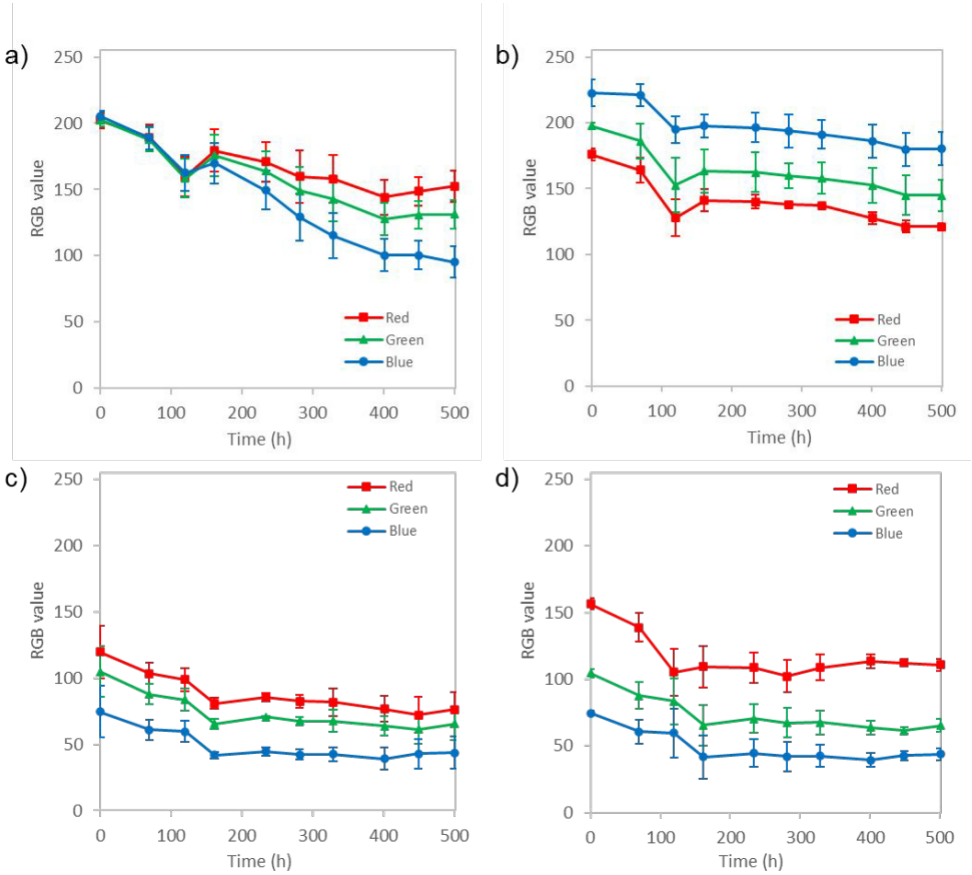

Figure 11. RGB evolution of four CNC film variants during 1000 h of solar aging. Panels **(a)**–**(d)** depict the separate R, G, and B channels for **(a)** BSK 58, **(b)** BSK 64, **(c)** UBSK 58, and **(d)** UBSK 64, respectively. Each dataset represents the mean of three distinct measurement areas on the film, with error bars indicating standard deviations. Adapted from the **publication III** SI under a CC BY 4.0 license.

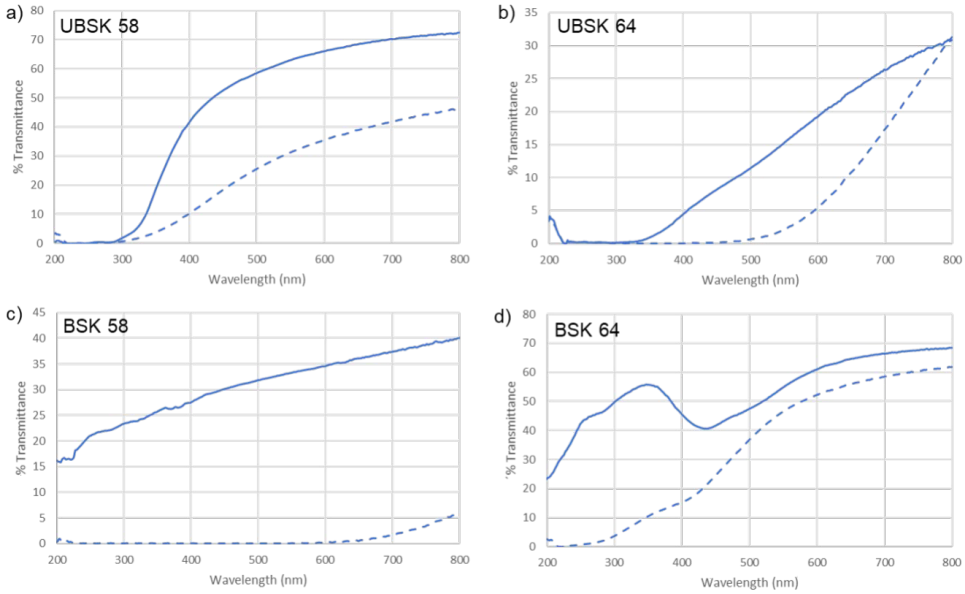

Figure 12. UV-Vis-NIR spectra of CNC films from bleached/unbleached pulps, comparing pre- and post-aging states. Each panel shows transmittance curves over 200–800 nm for one of the four variants before (solid line) and after (dashed line) 1000 h of simulated solar exposure. Note that Y axes are different for each subplot. Adapted from the **publication III** SI under a CC BY 4.0 license.

ture results stating that the sulfate half-ester groups introduced during acid hydrolysis are known to reduce the thermal stability of the films.[88] The UBSK 58 film darkened steadily without pronounced hue shifts, indicating the LNP, presented in the unbleached sample, improved UV stability compared to bleached samples (Figure 11c).

The UV-Vis-NIR spectra (Subsection 3.2.2) further supported these findings (Figure 12). The films made at the milder acid concentration, particularly BSK 58, displaying the most significant optical changes after aging. These changes included increased absorption in the visible range and more pronounced color inhomogeneities. For UBSK 64, already highly opaque in the UV due to lignin content, aging extended this opacity further into the visible region, up to 500 nm. The milder opacity shifts in UBSK 58 and BSK 64 suggest that higher cellulose crystallinity and possible lignin interactions slow, but do not prevent, photodegradation. UBSK 64 absorbed nearly all UV and a portion of visible light, confirming the role of lignin in initial optical filtering. In contrast, the BSK 58 film—despite lacking lignin—was unexpectedly less transparent than UBSK 58 and BSK 64, likely due to enhanced light scattering. Overall, these results demonstrate lignin's role in enhancing initial UV absorption while also contributing to opacity and structural changes under long-term solar exposure.

These results highlight how lignin content and acid concentration can directly impact CNC suspension rheology, film self-assembly, and long-term UV stability.

4.1.4 **Publication IV** Photostability of CNC:CNF hybrid films

Extending the exploration of bio-based films, the **publication IV** aimed to develop multifunctional NC-based films with tunable properties for different applications. The focused films consisted of CNC and CNF films in different mass ratios with and without sodium montmorillonite clay (MTM) (Subsection 3.1.1). MTM was integrated to enhance the films' water and oxygen barrier performance. (CNC:CNF):MTM films demonstrated improved barrier properties and notable resistance to swelling, making them ideal for packaging applications. CNC:CNF films without MTM exhibited exceptional optical properties with good color stability under prolonged exposure to artificial sunlight, making them suitable for photovoltaic applications.

To validate their potential for packaging applications, the barrier performance of the films was investigated through water vapor transmission rate (WVTR) tests. The results confirmed that incorporating MTM provided a relative improvement to the material's intrinsic barrier properties (Table 6). For instance, in the 50:50 CNC:CNF hybrid, the addition of MTM reduced the thickness-normalized WVTR from 3.3 to 2.4 g·mm/m^2·day. A similar improvement from 2.4 to 2.2 g·mm/m^2·day was observed for the pure CNF films containing MTM. It should be noted that measurements could not be performed on the pure CNC (100:0) films, both with and without MTM, as their brittle nature made them unsuitable for WVTR testing.

Table 6. WVTR of the select bio-based films containing. Measurements were conducted at 23℃ and 50% RH. Adapted from the **publication IV** under a CC BY 4.0 license.

CNC:CNF	Thickness (μm)	WVTR (g/m^2·day)	WVTR (g·mm/m^2·day)
50:50	22.9	144.20	3.3
50:50:MTM	18.6	133.10	2.4
0:100	30.9	76.57	2.4
0:100:MTM	23.9	90.38	2.2

Initial UV-Vis-NIR measurements (Subsection 3.2.2) showed that all CNC:CNF films were highly transparent across the visible spectrum (80% at 550 nm) with negligible UV-blocking properties (Figure 13a). Increasing the CNF content led to a marginal reduction in transmittance (>5%) and an increase in haze, likely due to the introduction of larger fibrils and voids within the film matrix. When 50 wt% MTM was added, films gained UV-shielding down to 250 nm while keeping visible transmittance between 60% and 80% depending on the CNC:CNF ratio (higher CNC,

higher transmittance). Also, the MTM presence increased haze for about 30% in films with higher CNC contents (100:0 and 75:25).

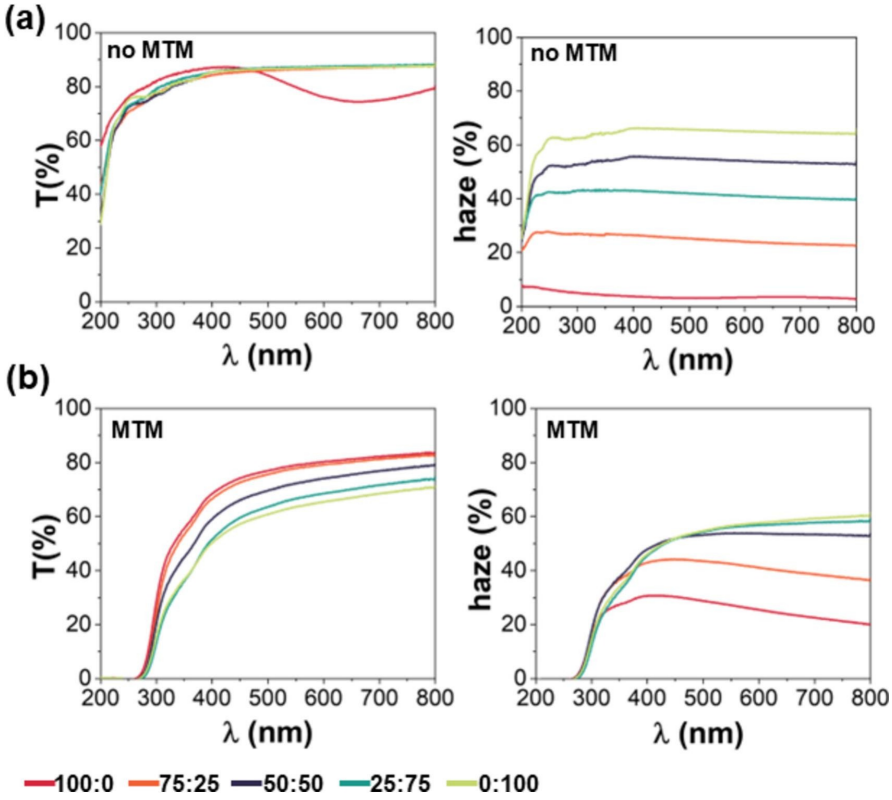

Figure 13. UV-Vis-NIR transmittance spectra of **(a)** CNC:CNF hybrid films without and **(b)** with MTM. Adapted from the **publication IV** under a CC BY 4.0 license.

High transparency in optoelectronics and resistance to discoloration for long-term packaging storage both depend critically on how these films withstand irradiation. To assess the color stability of CNC:CNF films, color alterations were monitored over 1800 h of artificial sunlight exposure (Subsections 3.2.1 and 3.2.4). The neat 100:0 CNC film was excluded from testing because its mechanical robustness was insufficient to endure the experimental conditions. Films containing MTM were also excluded due to their lower transparency and higher haze. All compositions demonstrated excellent color stability during the exposure period (Figure 14). Quantitative analysis showed minor color changes for all CNC:CNF ratios (Subsection 3.3.1). Minor fluctuations were mostly seen in the 75:25 CNC:CNF film, likely from surface reflections or slight repositioning during measurements.

Overall, CNC:CNF hybrid films without MTM showed high transparency, tunable haze, and excellent color stability, ideal for optoelectronics. Films containing MTM demonstrated moderate UV-blocking (below 250 nm), lower transparency,

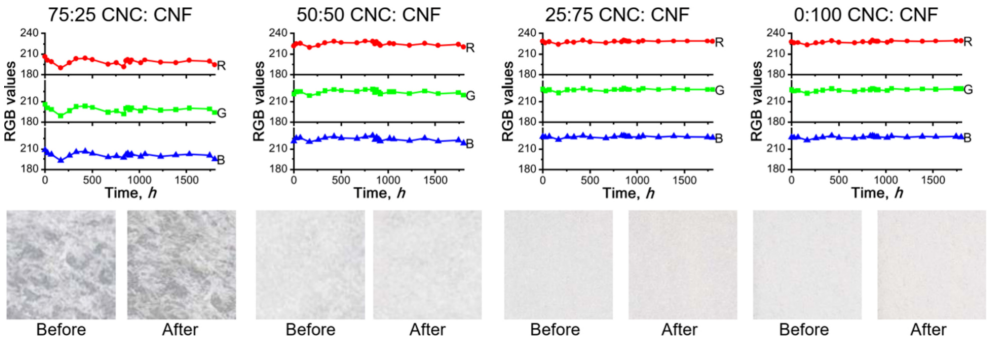

Figure 14. RGB channel values over 1800 h artificial solar exposure for CNC:CNF hybrid films, alongside visual appearance before and after aging, highlighting excellent color stability. Adapted from the **publication IV** under a CC BY 4.0 license.

and improved barrier properties, better suited for packaging applications where optical clarity is secondary.

4.2 **Publication V**: Self-cleaning and UV protective functional textiles

Based on previous successes with color tracking in NC-based films, the **publication V** focuses on cotton fabrics functionalized with ZnO nanostructures. This study examined how different synthesis conditions affect coating morphology, and thus UV stability and self-cleaning performance of the textile samples (Subsection 3.1.4). Different morphologies of ZnO, influencing surface area and photocatalytic efficiency, resulted in noticeable variations in stain removal capability and color retention. Such results indicate the possibility of optimizing fabric protection by tailoring the geometry of ZnO coatings.

The ZnO-coated fabrics were studied with UV-Vis-NIR spectroscopy (Subsection 3.2.2) and subsequently the UPF were calculated (Subsection 3.3.3). To evaluate the UV stability of the coatings, the measurements were done before and after the exposure to artificial sunlight (Subsection 3.2.1). The uncoated fabric, used as a reference, demonstrated that cotton material itself blocked approximately 98.5% of UV radiation (UPF=80.8) (Figure 15A and C, Table 7). All ZnO-coated samples presented even lower suppress transmission in the UV region, yielding UPF values from around 379 (0.3NaOH_50°C) up to 1000 (EtOH_Z) (Table 7). EtOH_Z delivers the highest protection (UPF=1039.9), which may be attributed to high crystal surface coverage. Post-aging spectra of ZnO-coated fabrics shows only approximately 1% shift in transmittance, although this variation can be attributed to natural variations in the sample, and the measurement process.

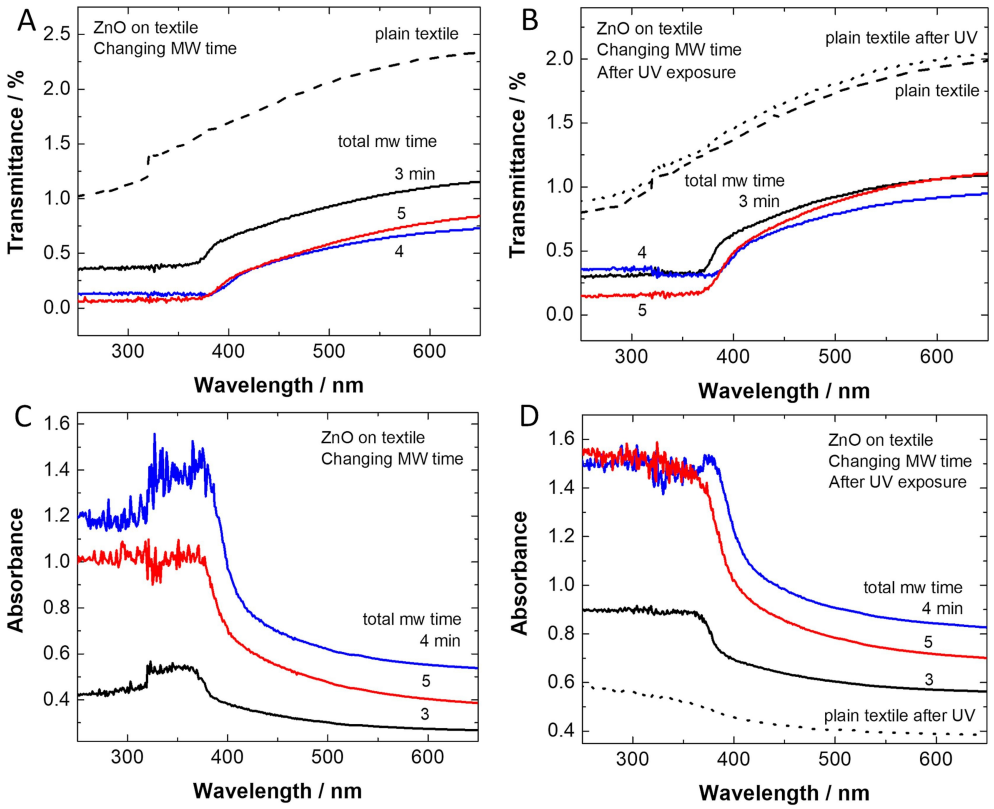

Figure 15. Transmittance and absorbance spectra of ZnO-coated cotton samples obtained using different microwaving times during the process, before (**A**,**C**) and after (**B**,**D**) aging tests. Adapted from the **publication V** under a CC BY 4.0 license.

Table 7. UPF protection metrics for ZnO-coated cotton samples. Adapted from the **publication V** SI under a CC BY 4.0 license.

Sample	UPF	UV-A Block (%)	UV-B Block (%)
Reference	80.8	98.5	98.8
0.1NaOH_30°C	589.4	99.8	99.9
0.1NaOH_t5	881.8	99.9	99.9
EtOH_Z	1039.9	99.9	99.9
0.3NaOH_50°C	379.5	99.8	99.8

To quantitatively assess self-cleaning performance, ZnO-functionalized fabrics were stained with MB and coffee, exposed to artificial sunlight, and analyzed via color tracking (Subsection 3.2.4). An uncoated fabric sample served as the baseline. Since the cotton fabric's color itself is around (200, 200, 200) in RGB, the presence of MB and coffee stains lowered this value significantly. Furthermore, the application of coatings led to different initial color intensities of the stains, a phenomenon attributed to variations in surface energies among the fabrics. Visually, all samples exhibited gradual lightening over exposure, indicating cotton material's sensitivity to UV exposure (Figure 16). Furthermore, the stains colors faded significantly across all samples, as evident by RGB values saturating towards higher values (Figure 16).

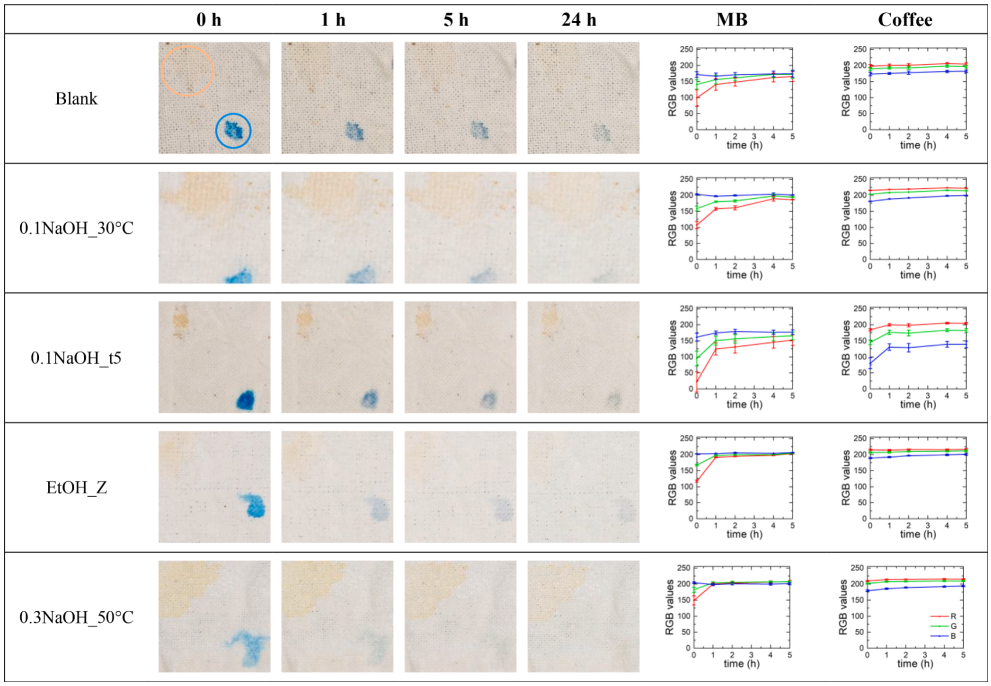

Figure 16. Time-series comparison of ZnO-coated cotton samples (Blank, 0.1NaOH_30℃, 0.1NaOH_t5, EtOH_Z, 0.3NaOH_50℃) stained with coffee (top left, orange circle) and MB (bottom right, blue circle), photographed at 0, 1, 5, and 24 h under artificial sunlight. Visual changes illustrate the self-cleaning process via progressive stain fading. Rightmost columns show RGB values as a function of time (up to 5 h) for both stains. Adapted from the **publication V** under a CC BY 4.0 license.

Stain removal efficiency was further assessed through quantifying the discoloration of MB stains (Subsection 3.3.1). The colors of the stained area were compared to the unstained area of the fabric, thus taking into account any color alterations of the fabric itself. Even the reference sample showed significant dye fading (33% after 1 h and 70% after 24 h), indicating inherent UV sensitivity (Table 8). Samples 0.1NaOH_30°C and 0.1NaOH_t5 showed moderate performance, achieving 40%

and 51% discoloration after 1 h, respectively, increasing to approximately 75% after 24 h. Superior results were observed for samples EtOH_Z and 0.3NaOH_50°C, which reached approximately 73% stain removal within the first hour and around 90% after 24 h.

Table 8. MB stain removal efficiency over time for various ZnO-coated textiles under solar exposure. Adapted from the **publication V** SI under a CC BY 4.0 license.

Time (h)	Reference	0.1NaOH_30°C	0.1NaOH_t5	EtOH_Z	0.3NaOH_50°C
1	33%	40%	51%	73%	72%
2	39%	42%	55%	75%	74%
4	49%	64%	60%	77%	78%
5	51%	62%	63%	82%	81%
24	71%	74%	77%	90%	84%
48	80%	89%	87%	92%	91%

Similarly, coffee stains provided insights into the practical stain resistance of the textiles (Table 9). The reference fabric only achieved 15% stain removal efficiency after 1 h with no significant improvement thereafter. Samples 0.1NaOH_30°C and 0.1NaOH_t5 were moderately effective, removing up to 64% and 60% after 24 h, respectively. Again, samples EtOH_Z and 0.3NaOH_50°C demonstrated superior results, with efficiencies of 82% and 67% at 24 h.

Table 9. Coffee stain removal efficiency as a function of exposure time to simulated sunlight. Adapted from the **publication V** SI under a CC BY 4.0 license.

Time (h)	Reference	0.1NaOH_30°C	0.1NaOH_t5	EtOH_Z	0.3NaOH_50°C
1	14%	22%	53%	18%	19%
2	6%	25%	57%	32%	23%
4	16%	40%	55%	44%	36%
5	12%	44%	54%	46%	41%
24	14%	64%	59%	82%	67%
48	31%	85%	75%	90%	75%

Overall, although flower-like morphologies (0.1NaOH_30°C, 0.1NaOH_t5) were initially predicted to offer the best self-cleaning due to elevated surface-to-volume ratios, practical results showed that other factors played a more significant role. For instance, the superior performance of samples EtOH_Z and 0.3NaOH_50°C underscored that effective photocatalysis relies on uniform ZnO coverage, optimal nanoparticle size and arrangement, and consequently, even surface distribution.

4.3 **Publication VI**: Simplifying PSC fabrication

Considering the previously discussed limitations of conventional FTO etching in PSC fabrication (Subsection 2.2.2), the **publication VI** introduces a simplified approach for producing and testing PSCs on unetched substrates (Subsection 3.1.3). Achieving this simplification involved using a custom-designed, 3D-printed holder equipped with spring-loaded contacts (pogo-pins) (Subsection 3.1.5). The holder itself provides reliable and scratch-free electrical contact, which is essential for using unetched substrates, as it reduces the main risk of short-circuiting that typically makes substrate etching necessary. Consequently, this approach enables researchers to rapidly prototype PSCs on a wide array of substrates while maintaining comparable performance to traditionally etched devices.

The solar cell samples were produced and divided into two groups based on the patterning of their bottom electrode, and their pixel distribution (Figure 17). When no etching was performed, the bottom conductive layer remains continuous across the device. Consequently, the top metal electrode (e.g., Au) must be patterned carefully to ensure it is electrically isolated and not short-circuited with the underlying unetched FTO. To achieve electrical isolation of the top electrodes on the continuous FTO layer, a portion of the mask was covered during deposition. This adaptation was implemented for the eight-pixel unetched device group Figure 17c, distinguishing it from the conventionally patterned etched version (Figure 17b).

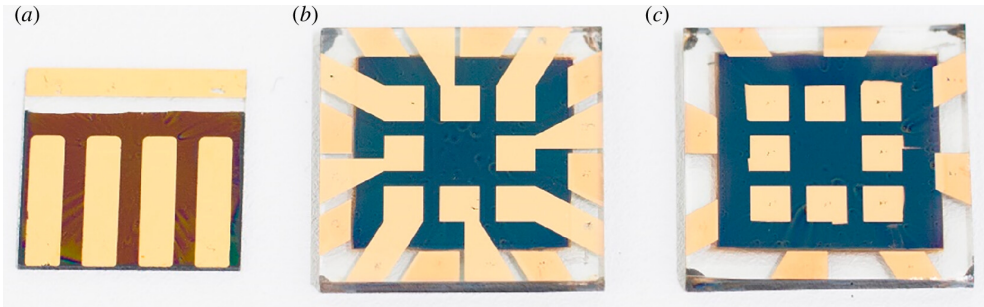

Figure 17. Digital images representing PSCs: (**a**) Four-pixel device with chemically etched FTO; (**b**) Eight-pixel device with laser-etched FTO; (**c**) Eight-pixel device with fully unetched FTO. Adapted from the **publication VI** under a CC BY 4.0 license.

With these individually defined top electrodes on the common unetched FTO, the 3D-printed holder then simplifies their electrical characterization (Figure 18). The holder consists of a base and a lid, which are attracted together with neodymium magnets securing the PSC. Integrated pogo pins make a gentle yet firm electrical connection with one pole contacting to a specific patterned top electrode of a single pixel, and another to the common FTO bottom conductive layer. This selective probing allows each pixel to be measured independently. Moreover, this direct contact method removes the need for conductive pastes and bypasses the conventional prac-

tice of extending contacts over non-conductive etched areas of the substrate. The lid further assists by stabilizing the PSC's position, thereby minimizing the risks of accidental short-circuits from scratches or probe misalignment during measurement.

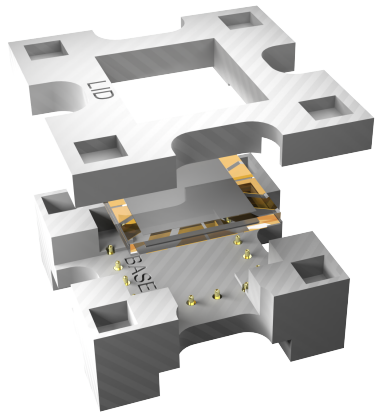

Figure 18. A 3D-rendered exploded view of the PSC holder system, demonstrating the arrangement of spring-loaded electrical contacts (pogo pins). This holder enables direct contacting of PSC electrodes, without etching or adding conductive pastes. Adapted from the **publication VI** SI under a CC BY 4.0 license.

To validate this simplified approach, the performance of PSCs on unetched substrates with those on conventionally etched ones was compared using JV measurements (Subsection 3.2.3). For the four-pixel layout, cells on unetched substrates measured from the edge (Edge U) demonstrated slightly higher short-circuit current densities (J_{SC} = $22.9 \pm 0.8\,\mathrm{mAcm^{-2}}$) compared to their etched counterparts (Edge E, J_{SC} = $22.1 \pm 0.8\,\mathrm{mAcm^{-2}}$) (Figure 19a). This difference in J_{SC} could be attributed to the way etching affects the subsequent gold deposition. In etched devices, the boundary created by FTO removal can lead to defects in the gold electrode. Conversely, the continuous FTO surface in unetched devices may allow for a more uniform gold electrode deposition, enhancing current extraction. Despite this minor J_{SC} difference, the overall power conversion efficiency (η) was nearly identical for both etched ($16.0 \pm 0.7\%$) and unetched ($16 \pm 1\%$) devices.

Further insights were gained by measuring the unetched cells from the center (Centre U). This aimed to determine if shortening the distance from the contact point to the active area affected performance, possibly due to series resistance. The results showed nearly identical efficiencies for edge ($16 \pm 1\%$) and center measurements ($16 \pm 2\%$), suggesting that increased series resistance from edge measurements does not substantially affect performance under these conditions.

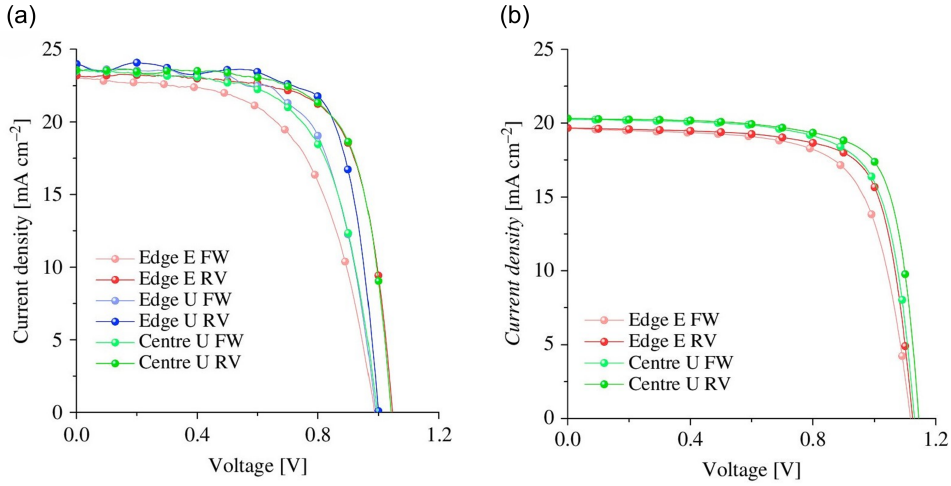

Figure 19. Comparison of JV characteristics for PSCs fabricated on etched and unetched substrates. **(a)** JV curves for a four-pixel PSC, comparing measurements on an etched substrate (Edge E) with those on an unetched substrate (Edge U, Centre U). **(b)** JV curves for an eight-pixel PSC, showing similar performance and minimal hysteresis between forward (FW) and reverse (RV) scans. The results for both layouts confirm that the unetched fabrication method does not penalize device performance. Adapted from the **publication VI** under a CC BY 4.0 license.

Similar behavior was confirmed with the eight-pixel layout shown in Figure 19b. Despite the more complex pixel geometry, the unetched devices exhibited comparable IV characteristics to their etched counterparts. A minor but noticeable improvement in FF was observed for unetched devices (increasing from $68\pm5\%$ to $72\pm4\%$), which slightly elevated their overall efficiencies compared to etched devices. This improvement could be associated with the lower series resistance (R_S), a benefit of contacting the pixel directly under the illuminated area.

In both four-pixel and eight-pixel layouts, minimal hysteresis between forward (FW) and reverse (RV) scans was observed. This underscores the reliability and consistency of measurements performed using the 3D-printed holder with spring-loaded pins.

Overall, these detailed observations strongly support the conclusion that removing FTO via chemical or laser etching is unnecessary for reliable and accurate device performance assessment at a research scale. This technique is especially valuable for testing PSCs on fragile substrates like NC, where traditional etching is often unfeasible or damaging.

4.4 Correlation between color changes and performance in solar cells

4.4.1 **Publication II**: DSSC electrolyte bleaching vs. performance

Beyond assessing their optical properties (Subsection 4.1.2), the **publication II** evaluated the long-term protective performance of the bio-based UV-filter films in practical application. To achieve this, the films were applied to DSSCs, which are known to be highly sensitive to UV radiation: such exposure can degrade a DSSC electrolyte, causing a distinctive color bleaching.[42] Such discoloration directly correlates with a reduced I_3^- concentration and signals a decline in the cell's electrical performance, particularly its J_{SC}.[44] This bleaching process was visually tracked to evaluate the practical UV protective efficiency of the filter films (Subsection 3.2.4)

DSSCs protected by CNF-ROE and commercial SFC-10 filters showed minimal bleaching over exposure, highlighting their superior UV-blocking capabilities (Figure 7). Notably, the DSSC shielded by the CNF-ROE filter maintained the most intense Y color of electrolyte, indicating the significant UV protection provided by this bio-based filter film. In contrast, unprotected solar cells exhibited the most severe bleaching, signifying extensive electrolyte degradation (Figure 7). The films containing iron ions (TOCNF-Fe^{3+}, TOCNF-ECH Fe^{3+}) offered poor UV shielding, with DSSCs under these films displayed considerable electrolyte bleaching. Finally, CNF-LNP offered moderate protection, but signs of degradation were noticeable, suggesting that although it provided some UV blocking, it was less effective compared to SFC-10 and CNF-ROE. These observations are closely aligned with the spectroscopy data discussed earlier (Figure 9): the higher the transmittance at the TiO_2 band gap, the more significant the electrolyte degradation and bleaching in DSSCs upon exposure (Figure 7).

Changes in the electrolyte Y value can serve as a more sensitive early indicator of degradation than J_{SC} itself (Subsection 3.2.3). This is because J_{SC} may only start to noticeably decrease after the initial excess of charge carriers in the electrolyte is significantly depleted and I_{lim} is reached. Thus, quantitative color analysis, focusing on the DSSCs electrolyte's Y intensity (Figure 8b), was performed to confirm its correlation with the cells' electrical performance (Figure 8c). J_{SC} was chosen as the primary electrical metric because it is directly influenced by the concentration of I_3^- redox species within the electrolyte, which ultimately limits the cell's maximum achievable current I_{lim}. In the experiments, most cells underwent an initial J_{SC} stabilization period of approximately 100 hours. However, unprotected cells and those under the least effective filters, such as TOCNF-ECH Fe^{3+}, degraded much faster, showing significant declines in both their Y value and J_{SC} within the first 24 to 75 hours. Conversely, DSSC shielded by the CNF-ROE filter demonstrated excellent J_{SC} stability throughout the test. Even the commercial SFC-10 filter, while per-

forming well initially, began to show rapid electrolyte bleaching, and a J_{SC} decline around the 900-hour mark.

Since several UV-filter films, notably CNF-ROE, CNF-LNP, and SFC-10, effectively protected DSSCs from rapid degradation within the 1000-hour test period, predictive modeling was employed (Subsection 3.3.2). This approach was used to forecast solar cells' longer-term performance under continued light exposure (Figure 20). Such modeling becomes particularly useful when projected device lifetimes extend beyond practical accelerated aging test durations. It uses the earlier observation that electrolyte bleaching (Figure 8b) is a sensitive indicator of I_3^- depletion, even while J_{SC} might remain stable until a critical limit of charge carriers is reached. The predictive model, based on the initial rate of electrolyte color alteration, therefore estimates device lifetime by focusing on these long-term degradation trends, excluding initial stabilization effects.[44]

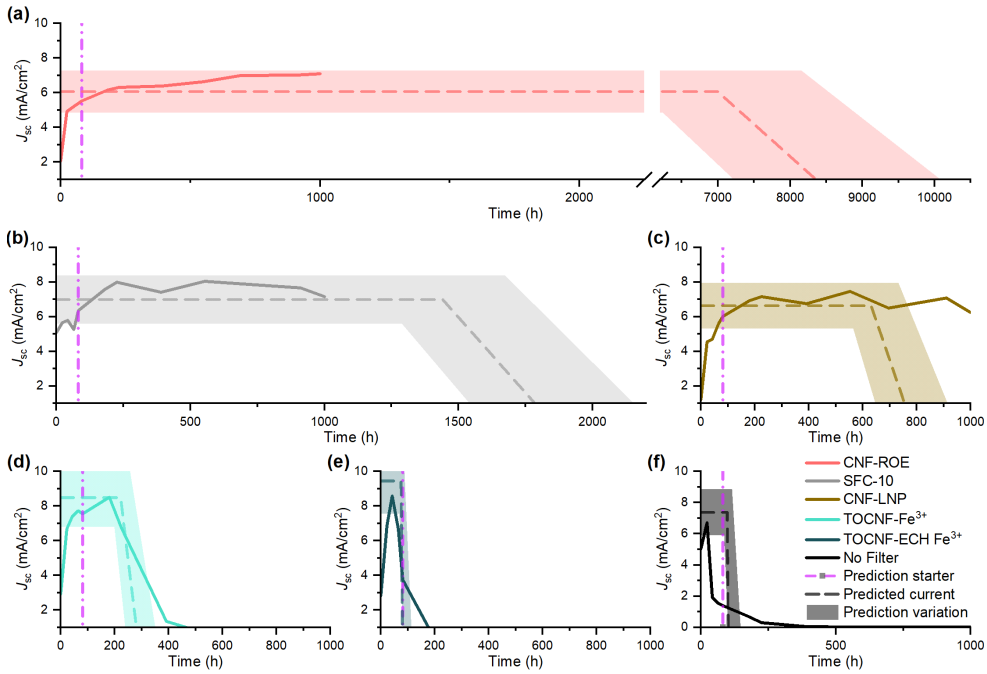

Figure 20. Predictive modeling of DSSC lifetime based on visual color changes in electrolytes protected by various UV-filter films. The models cover different filters: (**a**) CNF-ROE, (**b**) SFC-10, (**c**) CNF-LNP, (**d**) TOCNF-ECH Fe^{3+}, (**e**) TOCNF-Fe^{3+}, and (**f**) with no UV filter. Predictions are founded on color data captured within the initial 80 hours (purple dashed-dotted line). The horizontal dashed line and shaded areas represent the initial conditions. The colored areas in the predicted J_{SC} trends account for uncertainties, including inaccuracies in diffusion coefficient and charge carrier conversion. Shaded areas represent uncertainty bounds in predictions. Adapted from the **publication II** under a CC BY 4.0 license.

For DSSCs protected by the CNF-ROE filter film, this model projected an impressive operational lifetime of approximately 8500 hours (Figure 20a). This projected lifespan significantly surpassed that of a cell protected by the commercial SFC-10 filter, which were predicted to be operative effectively for only about 1500 hours (Figure 20b). The DSSC under the CNF-LNP film demonstrated a moderate predicted lifespan of around 700 hours (Figure 20c). In contrast, the TOCNF-based films (TOCNF-Fe^{3+} and TOCNF-ECH Fe^{3+}) offered insufficient UV protection. Their predictive data, showing very short operational times, closely resembled that of an entirely unprotected DSSC (Figure 20d, e, and f).

In summary, the detailed tracking of electrolyte color changes, combined with electrical performance metrics, provided compelling evidence for the practical protective effectiveness of these bio-based UV-filter films. Among all the tested films, the CNF-ROE filter uniquely demonstrated robust UV protection and exceptional photostability. These findings highlight red onion-based films as a promising sustainable option for UV protection in optoelectronic applications where material sustainability is important.

4.4.2 **Publication VII**: PSC lightening vs. performance

Finally, extending the color-monitoring approach, the **publication VII** applies a non-invasive imaging method to correlate the discoloration of PSCs with changes in their electrical performance. The method uses subtle color shifts, captured through digital imaging, to monitor degradation phenomena in the fabricated PSCs (Subsection 3.1.3). Unlike invasive characterization methods such as XRD or FESEM, this color-based approach simplifies long-term stability monitoring.

To establish a non-invasive degradation monitoring method for PSCs, color alterations were tracked using digital imaging methodology (Subsection 3.2.4) over the 9200 hours of dark storage (Subsection 3.2.1). Visual observations (Figure 21) revealed minimal color alteration in C-PSCs, which initially appeared nearly black and underwent only a slight color shift toward lighter shades. Although these color shifts were measurable, their magnitude remained below the human perceptual threshold for a just noticeable difference.[62] Notably, a yellowish discoloration pattern emerged around the active cell areas, likely associated with the formation of non-photoactive PbI_2.[89]

In contrast, Au-PSCs underwent degradation that resulted in significant changes to their visual appearance. Initially, the perovskite layers in these cells were as visually dark as those in C-PSCs (Figure 21). However, after approximately 1500 h of exposure, a distinct color shift became evident, progressing to significant discoloration by the end of the aging test. This marked visual degradation suggests extensive ion migration within Au-PSCs, potentially leading to perovskite decomposition.[48] Additional degradation pathways likely contributing to these color alterations include

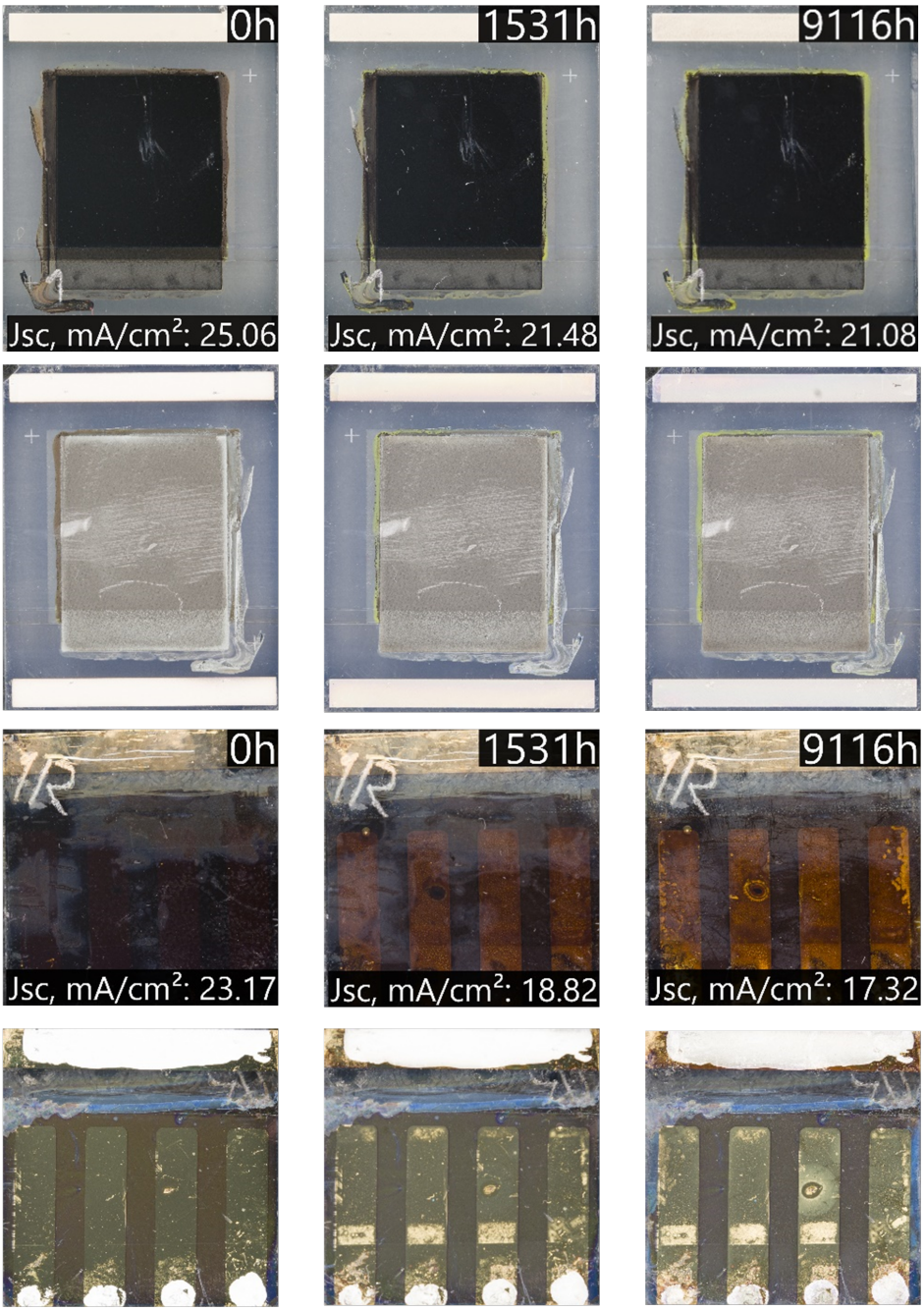

Figure 21. Periodic images of both sides of a C-PSC and Au-PSC, displaying color alterations within 9100 h of dark storage (ISOS-D-1). Adapted from the **publication VII**, originally published in the proceedings of the 41st European Photovoltaic Solar Energy Conference and Exhibition (EU PVSEC 2024, Vienna, Austria). Original publication: DOI: 10.4229/EU-PVSEC2024/2BV.1.29.

oxidation of the Spiro-OMeTAD hole transport layer, interactions between the gold electrodes and perovskite layers, and moisture-induced formation of yellowish PbI_2 and related compounds.[90] Moreover, uneven degradation across individual pixels was observed, underscoring that stability varied over the device area.

To quantify the visual changes observed and to investigate their relationship with device performance, quantitative color analysis was performed (Subsections 3.1.5, 3.2.3 and 3.3.1). This analysis using CIELAB and CIELCh channels correlated strongly with electrical performance metrics in both C-PSCs and Au-PSCs. For the C-PSCs, the b^* component of CIELAB displayed the strongest correlation with J_{SC}. Figure 22 presents the time evolution of η, V_{OC}, FF, and J_{SC} for a representative C-PSC over 9000 h, plotted alongside the measured b^*. Despite generally small color shifts, a simultaneous decline in b^* and J_{SC} emerges after the first few hundred hours, resulting in a significant correlation coefficient $r \approx 0.76$ and p-value of 0.019.

In the case of Au-PSCs, J_{SC} demonstrated a strong correlation with h° channel of CIELCh. Figure 23 presents the corresponding long-term performance data for an Au-PSC, illustrating the evolution of its color and performance metrics. The calculated average Pearson correlation coefficient between h° and J_{SC} for Au-PSCs was -0.67 with a p-value of 0.018, confirming a statistically significant negative linear relationship. Here, an increase in the h° value (a shift in hue) accompanies a 28% loss in J_{SC}. This aligns with prior findings that Au-PSCs degrade more severely due to ion migration and Spiro-OMeTAD oxidation.[47,90]

To further quantify the overall perceived color differences between the initial and aged states of the cells, the ΔE_{DIN99} was used. This metric is designed to reflect human perception of color change, with higher ΔE_{DIN99} values indicating more significant alterations. For Au-PSCs, the average ΔE_{DIN99} value was notably larger at 22.6, compared to a much smaller value of 2.8 for C-PSCs. This substantial difference in total color change aligns with the more pronounced visual alterations observed in Au-PSCs and is consistent with their greater reduction in J_{SC} during aging.

The subtle color alterations observed in C-PSCs suggest the carbon electrode offers considerable protection, though eventual degradation is still noted.[89,91] In contrast, Au-PSCs showed much faster and more visually pronounced perovskite breakdown. The distinct visual degradation patterns in the two cell types highlight how color monitoring can help compare the stability offered by different electrode materials.

Overall, unlike in DSSCs, where early color shifts can precede efficiency loss and enable prediction, color changes in these PSCs occurred concurrently with electrical performance decline. Though color predictions for long-term performance remain challenging, the strong correlations highlight the practicality of digital imaging as a simple, non-invasive monitoring approach for PSCs under prolonged aging.

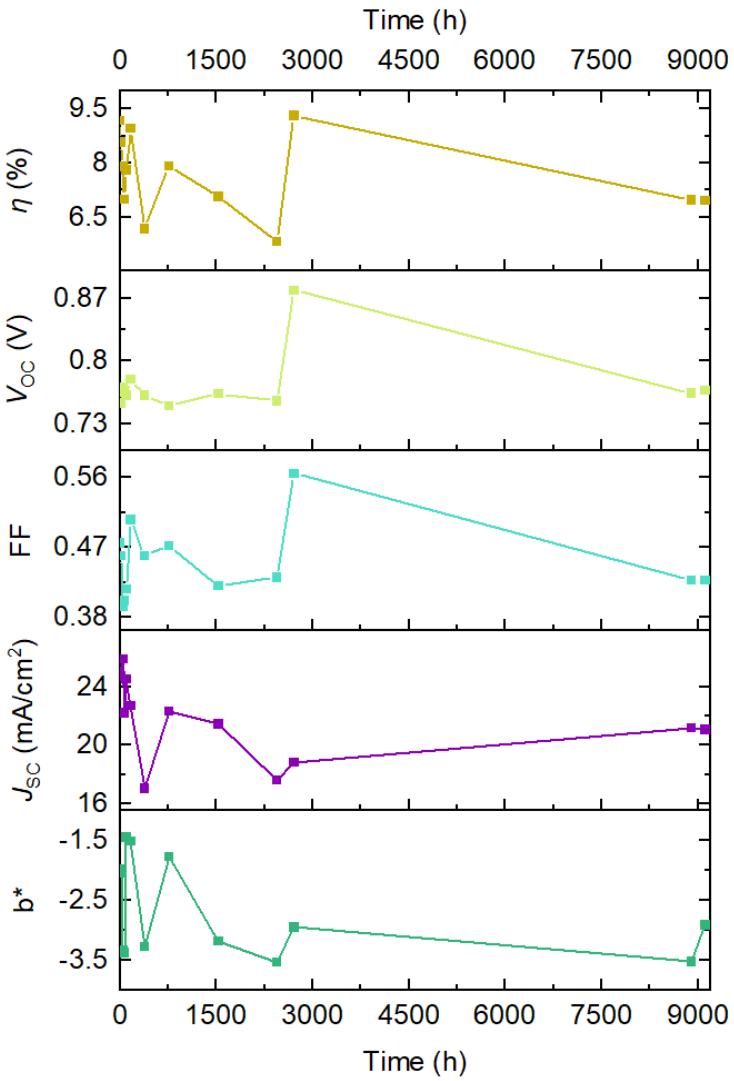

Figure 22. Long-term evolution of η, V_{OC}, FF, and J_{SC} for a representative C-PSC over 9000 h of storage, alongside the measured b^* parameter. The close trend between η (gold squares) and b^* (green squares) confirms that color changes, although small, track performance losses in the carbon-based device. Adapted from the **publication VII**, originally published in the proceedings of the 41st European Photovoltaic Solar Energy Conference and Exhibition (EU PVSEC 2024, Vienna, Austria). Original publication: DOI: 10.4229/EUPVSEC2024/2BV.1.29.

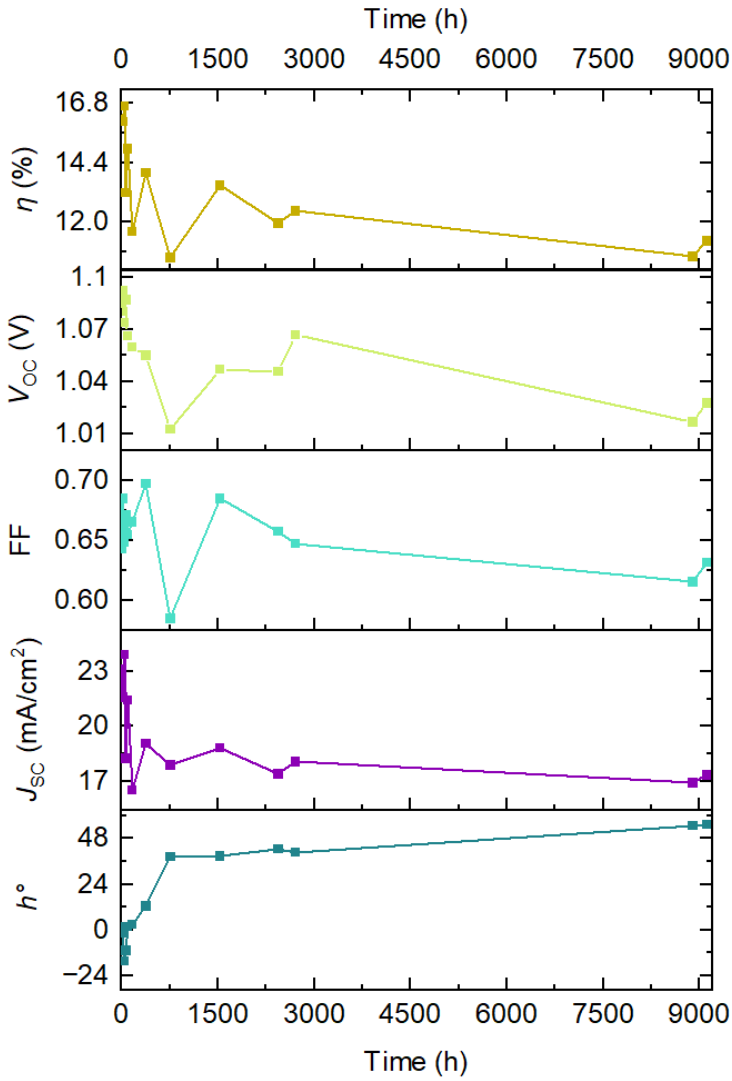

Figure 23. Corresponding long-term performance of an Au-PSC, showing η, V_{OC}, FF, and J_{SC} along with the h° parameter. Here, h° (blue squares) rises as J_{SC} (purple squares) decreases, consistent with more severe degradation pathways in Au-based cells compared to their carbon counterparts. Adapted from the **publication VII**, originally published in the proceedings of the 41st European Photovoltaic Solar Energy Conference and Exhibition (EU PVSEC 2024, Vienna, Austria). Original publication: DOI: 10.4229/EUPVSEC2024/2BV.1.29.

5 Conclusions and future work

This dissertation investigated the stability of various sustainable materials and photovoltaic devices under prolonged aging conditions, with special emphasis on a color-based approach for non-invasive degradation assessment. The research demonstrates how digital photography, combined with controlled lighting and color-space conversions, can reliably detect subtle color alterations that correlate with underlying chemical or morphological changes in the studied materials and devices. This methodology provides a straightforward and resource-efficient framework for evaluating and comparing the stability of these systems over time.

5.1 Summary of key contributions

A significant portion of this work focused on assessing and enhancing the UV stability of NC-based films. Investigations into lignin-incorporated NC films (**publication I**) established that lignin, whether present as a residual component or as added nanoparticles, provides robust and durable UV-shielding properties that are essential for optoelectronic applications. Further exploration of bio-based UV filters involved applying various modified NC films to DSSCs (**publication II**). Among these filters, a CNF film dyed with red onion extract demonstrated exceptional UV-blocking capabilities and superior durability, outperforming other bio-filters and a commercial reference. Studies also delved into how processing conditions, such as acid hydrolysis parameters and pulp source, affect the photostability and properties of crystalline lignocellulose isolates, showing that these factors can be tuned to tailor film characteristics (**publication III**). Additionally, hybrid films combining CNC and CNF, with and without MTM clay, were developed; neat CNC:CNF films showed excellent transparency and color stability for optoelectronics, while clay-containing variants offered improved barrier properties and UV-shielding suitable for packaging (**publication IV**). The color alteration monitoring was applied to ZnO functional textiles, where ZnO morphologies significantly enhanced the cotton fabric's UV protection and photocatalytic self-cleaning performance (**publication V**).

Finally, this dissertation addressed challenges in PSC research. A notable contribution was the development of a 3D-printed holder that simplifies PSC fabrication and testing by enabling the use of unetched FTO substrates (**publication VI**). Further work applied non-invasive imaging to correlate discoloration with electrical perfor-

mance decline in C-PSCs and Au-PSCs over extended dark storage (**publication VII**). A key finding here was that color alterations in these PSCs occurred simultaneously with their electrical performance degradation. This established the color-based method as a valuable real-time indicator of ongoing degradation in PSCs, in contrast to its predictive capability observed in DSSCs where color changes preceded performance loss.

Collectively, these studies establish color alteration as a versatile and reliable indicator of degradation across a diverse range of sustainable materials and photovoltaic devices. The development of simplified fabrication tools, and the application of non-invasive monitoring techniques both contribute practical, low-cost solutions to advancing the stability of these systems.

5.2 Limitations and challenges

Although this dissertation demonstrates the broad applicability of color-based degradation monitoring, the methodologies employed have certain limitations and challenges. A primary consideration is that the color analysis conducted did not utilize a standardized illuminant, such as D65, for image capture. Consequently, while the observed trends are internally consistent due to uniform conditions maintained throughout this study, absolute color values could vary under different lighting environments. This may require a careful calibration for direct comparison of results across diverse experimental setups or future industrial implementations. Furthermore, the color-monitoring approach is predominantly surface-sensitive. Consequently, it might not detect subsurface degradation phenomena if such internal changes do not appear as externally visible color alterations in the materials or devices.

Another important aspect concerns the differing nature of the correlation between color and performance across various photovoltaic technologies. The predictive power of color change as an early indicator of failure, clearly observed in DSSCs where electrolyte bleaching often preceded significant efficiency loss, was found to be diminished in the studied PSCs. For these perovskite devices, color alterations and electrical performance degradation occurred synchronously.

These points indicate that while color-based monitoring is a powerful tool, its application and interpretation require careful consideration of the specific system and measurement context.

5.3 Future research directions

Building upon the findings and limitations identified in this work, several avenues for future research emerge that could potentially be studied and employed. A crucial next step would be the systematic integration of standardized illumination, such as D65, into the image capture protocol. This would greatly improve the inter-

laboratory comparability and absolute accuracy of colorimetric data, addressing a key limitation of the current studies. Exploring the use of complementary imaging or spectroscopic techniques in conjunction with color analysis also presents a promising direction. For instance, infrared thermography could reveal thermal non-uniformities indicative of degradation, while UV fluorescence imaging might uncover chemical changes not revealed in the visible spectrum, thus providing a more holistic understanding of degradation mechanisms.

Conducting long-term outdoor aging studies, in parallel with laboratory-based accelerated tests, would be invaluable for correlating the observed color changes with real-world operational stability and environmental stressors. Beyond these experimental refinements, significant potential lies in developing more sophisticated data analysis techniques. One prospective direction is to embed automated image processing, potentially harnessing machine learning algorithms, to detect subtle or complex color shifts in real time. Such systems could learn to identify specific degradation signatures from evolving color patterns and generate immediate alerts if material or device performance risks exceeding critical thresholds. Advancing these research lines could further solidify color-based analysis as a simple, yet powerful, and cost-effective tool for monitoring material durability, which is essential for the continued development of sustainable energy technologies.

List of References

[1] Erich M Fischer and Reto Knutti. Anthropogenic contribution to global occurrence of heavy-precipitation and high-temperature extremes. *Nature climate change*, 5(6):560–564, 4 2015. ISSN 1758-678X. doi: 10.1038/nclimate2617.

[2] Sonia I Seneviratne, Markus G Donat, Andy J Pitman, Reto Knutti, and Robert L Wilby. Allowable CO_2 Emissions Based on Regional and Impact-Related Climate Targets. *Nature*, 529(7587): 477–483, 1 2016. ISSN 0028-0836. doi: 10.1038/nature16542.

[3] AG Olabi and Mohammad Ali Abdelkareem. Renewable energy and climate change. *Renewable and Sustainable Energy Reviews*, 158:112111, 4 2022. ISSN 1364-0321. doi: 10.1016/j.rser.2022.112111.

[4] Kati Miettunen, Mahboubeh Hadadian, Joaquín Valdez García, Alicja Lawrynowicz, Elena Akulenko, Orlando J. Rojas, Michael Hummel, and Jaana Vapaavuori. Bio-based materials for solar cells. *WIREs Energy and Environment*, 13(1):e508, 1 2024. ISSN 2041-8396. doi: 10.1002/wene.508.

[5] Carolina Rodrigues, Victor Gomes Lauriano Souza, Isabel Coelhoso, and Ana Luísa Fernando. Bio-Based Sensors for Smart Food Packaging—Current Applications and Future Trends. *Sensors*, 21(6):2148, 3 2021. ISSN 1424-8220. doi: 10.3390/s21062148.

[6] Reza Yekta, Reza Abedi-Firoozjah, Shamimeh Azimi Salim, Arezou Khezerlou, and Khadije Abdolmaleki. Application of cellulose and cellulose derivatives in smart/intelligent bio-based food packaging. *Cellulose*, 30(16):9925–9953, 9 2023. ISSN 0969-0239. doi: 10.1007/s10570-023-05520-1.

[7] Anthony L Andrady, AM Heikkilä, KK Pandey, LS Bruckman, CC White, M Zhu, and L Zhu. Effects of UV radiation on natural and synthetic materials. *Photochemical & Photobiological Sciences*, 22(5):1177–1202, 4 2023. ISSN 1474-905X. doi: 10.1007/s43630-023-00377-6.

[8] Wei Liu, Kun Liu, Haishun Du, Ting Zheng, Ning Zhang, Ting Xu, Bo Pang, Xinyu Zhang, Chuanling Si, and Kai Zhang. Cellulose nanopaper: fabrication, functionalization, and applications. *Nano-Micro Letters*, 14(1):104, 4 2022. ISSN 2150-5551. doi: 10.1007/s40820-022-00849-x.

[9] Dawei Zhao, Ying Zhu, Wanke Cheng, Wenshuai Chen, Yiqiang Wu, and Haipeng Yu. Cellulose-Based Flexible Functional Materials for Emerging Intelligent Electronics. *Advanced Materials*, 33(28):2000619, 7 2021. ISSN 0935-9648. doi: 10.1002/adma.202000619.

[10] Kati Miettunen and Annukka Santasalo-Aarnio. Eco-design for dye solar cells: From hazardous waste to profitable recovery. *Journal of Cleaner Production*, 320:128743, 8 2021. ISSN 0959-6526. doi: 10.1016/j.jclepro.2021.128743.

[11] Elena S Akulenko, Mahboubeh Hadadian, Annukka Santasalo-Aarnio, and Kati Miettunen. Eco-design for perovskite solar cells to address future waste challenges and recover valuable materials. *Heliyon*, 9(2):e13584, 2 2023. ISSN 2405-8440. doi: 10.1016/j.heliyon.2023.e13584.

[12] Albert Serra, Israel González, Helena Oliver-Ortega, Quim Tarrès, Marc Delgado-Aguilar, and Pere Mutjé. Reducing the amount of catalyst in TEMPO-oxidized cellulose nanofibers: Effect on properties and cost. *Polymers*, 9(11):557, 10 2017. ISSN 2073-4360. doi: 10.3390/polym9110557.

[13] Seth Kane, Sabbie A Miller, Kimberly E Kurtis, Jeffrey P Youngblood, Eric N Landis, and W Jason Weiss. Harmonized life-cycle inventories of nanocellulose and its application in composites.

Environmental Science & Technology, 57(48):19137–19147, 11 2023. ISSN 0013-936X. doi: 10.1021/acs.est.3c04814.

[14] Kelsey AW Horowitz, Ran Fu, and Michael Woodhouse. An analysis of glass–glass CIGS manufacturing costs. *Solar Energy Materials and Solar Cells*, 154:1–10, 4 2016. ISSN 0927-0248. doi: 10.1016/j.solmat.2016.04.029.

[15] Coenraad D Westbroek, Jennifer Bitting, Matteo Craglia, José MC Azevedo, and Jonathan M Cullen. Global material flow analysis of glass: From raw materials to end of life. *Journal of Industrial Ecology*, 25(2):333–343, 3 2021. ISSN 1088-1980. doi: 10.1111/jiec.13112.

[16] Joice Jaqueline Kaschuk, Yazan Al Haj, Orlando J Rojas, Kati Miettunen, Tiffany Abitbol, and Jaana Vapaavuori. Plant-based structures as an opportunity to engineer optical functions in next-generation light management. *Advanced Materials*, 34(6):2104473, 2022. doi: 10.1002/adma.202104473.

[17] Sung Min Moon, Dong-Wook Kim, Seunghyeon Lee, Taesik Eom, So Hui Jeon, and Bong Sup Shim. Precisely tuned photonic properties of crystalline nanocellulose biocomposite coatings by gradually tailored nanoarchitectures. *Carbohydrate Polymers*, 282:119053, 1 2022. ISSN 0144-8617. doi: 10.1016/j.carbpol.2021.119053.

[18] Gabriel Banvillet, Clément Grange, Denis Curtil, Jean-Luc Putaux, Gaël Depres, Naceur Belgacem, and Julien Bras. Cellulose nanofibril production by the combined use of four mechanical fibrillation processes with different destructuration effects. *Cellulose*, 30(4):2123–2146, 1 2023. ISSN 0969-0239. doi: 10.1007/s10570-022-05016-4.

[19] Ao Li, Dezhong Xu, Lu Luo, Yalan Zhou, Wen Yan, Xin Leng, Dasong Dai, Yonghui Zhou, Hassan Ahmad, Jiuping Rao, et al. Overview of nanocellulose as additives in paper processing and paper products. *Nanotechnology Reviews*, 10(1):264–281, 2021. ISSN 2191-9089. doi: 10.1515/ntrev-2021-0023.

[20] J. Malešič, J. Kolar, M. Strlič, D. Kočar, D. Fromageot, J. Lemaire, and O. Haillant. Photo-induced degradation of cellulose. *Polymer Degradation and Stability*, 89(1):64–69, 2005. ISSN 0141-3910. doi: doi.org/10.1016/j.polymdegradstab.2005.01.003.

[21] Tsuguyuki Saito, Satoshi Kimura, Yoshiharu Nishiyama, and Akira Isogai. Cellulose nanofibers prepared by TEMPO-mediated oxidation of native cellulose. *Biomacromolecules*, 8(8):2485–2491, 7 2007. ISSN 1525-7797. doi: 10.1021/bm0703970.

[22] Qianqiu Xing, David Ruch, Philippe Dubois, Linbo Wu, and Wen-Jun Wang. Biodegradable and high-performance poly (butylene adipate-co-terephthalate)–lignin UV-blocking films. *ACS Sustainable Chemistry & Engineering*, 5(11):10342–10351, 2017. doi: 10.1021/acssuschemeng.7b02370.

[23] Naresh Shahi, Eunji Lee, Byungjin Min, and Dong-Joo Kim. Rice Husk-Derived Cellulose Nanofibers: A Potential Sensor for Water-Soluble Gases. *Sensors*, 21(13), 2021. ISSN 1424-8220. doi: 10.3390/s21134415.

[24] Weisheng Yang, Xiu Wang, Parikshit Gogoi, Huiyang Bian, and Hongqi Dai. Highly transparent and thermally stable cellulose nanofibril films functionalized with colored metal ions for ultraviolet blocking activities. *Carbohydrate Polymers*, 213:10–16, 6 2019. ISSN 01448617. doi: 10.1016/j.carbpol.2019.02.085.

[25] Eva Pasquier, Bruno D Mattos, Naceur Belgacem, Julien Bras, and Orlando J Rojas. Lignin nanoparticle nucleation and growth on cellulose and chitin nanofibers. *Biomacromolecules*, 22(2):880–889, 12 2020. ISSN 1525-7797. doi: 10.1021/acs.biomac.0c01596.

[26] Rafael Grande, Riikka Räisänen, Jinze Dou, Satu Rajala, Kiia Malinen, Paula A. Nousiainen, and Monika Österberg. In situ adsorption of red onion (*Allium cepa*) natural dye on cellulose model films and fabrics exploiting chitosan as a natural mordant. *ACS Omega*, 8(6):5451–5463, 2 2023. ISSN 24701343. doi: 10.1021/acsomega.2c06650.

[27] Dingfeng Xu, Shennan Wang, Lars A Berglund, and Qi Zhou. Surface charges control the structure and properties of layered nanocomposite of cellulose nanofibrils and clay platelets. *ACS applied materials & interfaces*, 13(3):4463–4472, 1 2021. ISSN 1944-8244. doi: 10.1021/acsami.0c18594.

[28] Brian O'regan and Michael Grätzel. A low-cost, high-efficiency solar cell based on dye-sensitized colloidal TiO2 films. *nature*, 353(6346):737–740, 10 1991. ISSN 0028-0836. doi: 10.1038/353737a0.

[29] Nam-Gyu Park. Perovskite solar cells: an emerging photovoltaic technology. *Materials Today*, 18(2):65–72, 2015. ISSN 1369-7021. doi: 10.1016/j.mattod.2014.07.007.

[30] International Electrotechnical Commission. Terrestrial Photovoltaic (PV) Modules – Design Qualification and Type Approval – Part 1: Test Requirements (Redline Version), 2021. URL https://webstore.iec.ch/en/publication/68594. Includes both the official IEC standard and a redline comparison with IEC 61215-1:2016.

[31] Matthew O Reese, Suren A Gevorgyan, Mikkel Jørgensen, Eva Bundgaard, Sarah R Kurtz, David S Ginley, Dana C Olson, Matthew T Lloyd, Pasquale Morvillo, Eugene A Katz, et al. Consensus stability testing protocols for organic photovoltaic materials and devices. *Solar Energy Materials and Solar Cells*, 95(5):1253–1267, 3 2011. ISSN 0927-0248. doi: 10.1016/j.solmat.2011.01.036.

[32] Mark V Khenkin, Eugene A Katz, Antonio Abate, Giorgio Bardizza, Joseph J Berry, Christoph Brabec, Francesca Brunetti, Vladimir Bulović, Quinn Burlingame, Aldo Di Carlo, et al. Consensus statement for stability assessment and reporting for perovskite photovoltaics based on ISOS procedures. *Nature Energy*, 5(1):35–49, 1 2020. ISSN 2058-7546. doi: 10.1038/s41560-019-0529-5.

[33] Rui Wang, Muhammad Mujahid, Yu Duan, Zhao-Kui Wang, Jingjing Xue, and Yang Yang. A review of perovskites solar cell stability. *Advanced Functional Materials*, 29(47):1808843, 2019. doi: doi.org/10.1002/adfm.201808843.

[34] Janne Halme, Paula Vahermaa, Kati Miettunen, and Peter Lund. Device physics of dye solar cells. *Advanced materials*, 22(35):E210–E234, 8 2010. ISSN 0935-9648. doi: 10.1002/adma.201000726.

[35] Reena Kushwaha, Pankaj Srivastava, and Lal Bahadur. Natural Pigments from Plants Used as Sensitizers for TiO2 Based Dye-Sensitized Solar Cells. *International Journal of Photoenergy*, 2013:654953, 2013. doi: 10.1155/2013/654953.

[36] Brian O'Regan and Michael Grätzel. A low-cost, high-efficiency solar cell based on dye-sensitized colloidal TiO2 films. *Nature*, 353(6346):737–740, 10 1991. ISSN 00280836. doi: 10.1038/353737a0.

[37] Marina Freitag, Joël Teuscher, Yasemin Saygili, Xiaoyu Zhang, Fabrizio Giordano, Paul Liska, Jianli Hua, Shaik M Zakeeruddin, Jacques-E Moser, Michael Grätzel, et al. Dye-sensitized solar cells for efficient power generation under ambient lighting. *Nature Photonics*, 11(6):372–378, 5 2017. ISSN 1749-4885. doi: 10.1038/nphoton.2017.60.

[38] Kati Miettunen, Jaana Vapaavuori, Aapo Poskela, Armi Tiihonen, and Peter D Lund. Recent progress in flexible dye solar cells. *Wiley Interdisciplinary Reviews: Energy and Environment*, 7(5):e302, 5 2018. ISSN 2041-8396. doi: 10.1002/wene.302.

[39] Jason B. Baxter. Commercialization of dye sensitized solar cells: Present status and future research needs to improve efficiency, stability, and manufacturing. *Journal of Vacuum Science & Technology A*, 30(2):020801, 02 2012. ISSN 0734-2101. doi: 10.1116/1.3676433.

[40] Ana Belén Muñoz-García, Iacopo Benesperi, Gerrit Boschloo, Javier J Concepcion, Jared H Delcamp, Elizabeth A Gibson, Gerald J Meyer, Michele Pavone, Henrik Pettersson, Anders Hagfeldt, et al. Dye-sensitized solar cells strike back. *Chemical Society Reviews*, 50(22):12450–12550, 2021. doi: doi.org/10.1039/D0CS01336F.

[41] Simone Mastroianni, Imran Asghar, Kati Miettunen, Janne Halme, Alessandro Lanuti, Thomas M. Brown, and Peter Lund. Effect of electrolyte bleaching on the stability and performance of dye solar cells. *Physical Chemistry Chemical Physics*, 16(13):6092, 3 2014. ISSN 14639076. doi: 10.1039/c3cp55342f.

[42] Aapo Poskela, Kati Miettunen, Armi Tiihonen, and Peter D. Lund. Extreme sensitivity of dye solar cells to UV-induced degradation. *Energy Science and Engineering*, 9:19–26, 1 2021. ISSN 20500505. doi: 10.1002/ese3.810.

[43] Leo Furnell, Peter J Holliman, Arthur Connell, Eurig W Jones, Robert Hobbs, Christopher P Kershaw, Rosie Anthony, Justin Searle, Trystan Watson, and James McGettrick. Digital imaging to simultaneously study device lifetimes of multiple dye-sensitized solar cells. *Sustainable Energy & Fuels*, 1(2):362–370, 2017. doi: 10.1039/C7SE00015D.

[44] Aapo Poskela, Armi Tiihonen, Heikki Palonen, Peter D. Lund, and Kati Miettunen. Predictive Modeling of Dye Solar Cell Degradation. *Solar RRL*, 6(6), 2 2022. ISSN 2367198X. doi: 10.1002/solr.202101004.

[45] Shangshang Chen, Xuezeng Dai, Shuang Xu, Haoyang Jiao, Liang Zhao, and Jinsong Huang. Stabilizing perovskite-substrate interfaces for high-performance perovskite modules. *Science*, 373(6557):902–907, 8 2021. ISSN 0036-8075. doi: 10.1126/science.abi6323.

[46] Martin A Green, Anita Ho-Baillie, and Henry J Snaith. The emergence of perovskite solar cells. *Nature photonics*, 8(7):506–514, 6 2014. ISSN 1749-4885. doi: 10.1038/nphoton.2014.134.

[47] Chuang Yang, Wenjing Hu, Jiale Liu, Chuanzhou Han, Qiaojiao Gao, Anyi Mei, Yinhua Zhou, Fengwan Guo, and Hongwei Han. Achievements, challenges, and future prospects for industrialization of perovskite solar cells. *Light: Science & Applications*, 13(1):227, 9 2024. ISSN 2047-7538. doi: 10.1038/s41377-024-01461-x.

[48] Jin-Wook Lee, Seul-Gi Kim, June-Mo Yang, Yang Yang, and Nam-Gyu Park. Verification and mitigation of ion migration in perovskite solar cells. *APL materials*, 7(4), 4 2019. ISSN 2166-532X. doi: 10.1063/1.5085643.

[49] Dian Wang, Matthew Wright, Naveen Kumar Elumalai, and Ashraf Uddin. Stability of perovskite solar cells. *Solar Energy Materials and Solar Cells*, 147:255–275, 1 2016. ISSN 0927-0248. doi: 10.1016/j.solmat.2015.12.025.

[50] Hongwei Zhu, Sam Teale, Muhammad Naufal Lintangpradipto, Suhas Mahesh, Bin Chen, Michael D McGehee, Edward H Sargent, and Osman M Bakr. Long-term operating stability in perovskite photovoltaics. *Nature Reviews Materials*, 8(9):569–586, 8 2023. ISSN 2058-8437. doi: 10.1038/s41578-023-00582-w.

[51] Shuhui Li, Jianying Huang, Zhong Chen, Guoqiang Chen, and Yuekun Lai. A review on special wettability textiles: theoretical models, fabrication technologies and multifunctional applications. *Journal of Materials Chemistry A*, 5(1):31–55, 2017. ISSN 2050-7496. doi: 10.1039/c6ta07984a.

[52] Thirumalaisamy Suryaprabha and Mathur Gopalakrishnan Sethuraman. A facile approach for fabrication superhydrophobic and UV-blocking cotton fabrics with self-cleaning properties. *Fibers and polymers*, 22(4):1033–1040, 3 2021. ISSN 1229-9197. doi: 10.1007/s12221-021-0648-z.

[53] Nasrin Talebian, Seyedeh Matin Amininezhad, and Monir Doudi. Controllable synthesis of ZnO nanoparticles and their morphology-dependent antibacterial and optical properties. *Journal of Photochemistry and Photobiology B: Biology*, 120:66–73, 2 2013. ISSN 1011-1344. doi: 10.1016/j.jphotobiol.2013.01.004.

[54] Ling Zhu, Yanqiong Li, and Wen Zeng. Hydrothermal synthesis of hierarchical flower-like ZnO nanostructure and its enhanced ethanol gas-sensing properties. *Applied Surface Science*, 427:281–287, 2018. ISSN 0169-4332. doi: 10.1016/j.apsusc.2017.08.229.

[55] Jacek Wojnarowicz, Tadeusz Chudoba, and Witold Lojkowski. A review of microwave synthesis of zinc oxide nanomaterials: Reactants, process parameters and morphologies. *Nanomaterials*, 10(6):1086, 5 2020. ISSN 2079-4991. doi: 10.3390/nano10061086.

[56] Mark D Fairchild. *Color appearance models*. John Wiley & Sons, 2013.

[57] Commission Internationale de l'Eclairage (CIE). *Colorimetry, 3rd Edition*. CIE Central Bureau, Vienna, Austria, 2004. ISBN 978-3-901-90633-6. URL https://cie.co.at/publications/colorimetry-3rd-edition.

[58] International Organization for Standardization. Colorimetry – Part 4: CIE 1976 Lab Colour Space, 2008. URL https://www.iso.org/standard/40879.html. Also published as CIE S 014-4/E:2007.

[59] International Organization for Standardization. Colorimetry – Part 2: CIE standard illuminants, 2007. URL https://www.iso.org/standard/44712.html.

[60] E Rohner and DC Rich. Eine angenahert gleichformige Metrik fur industrielle Farbtoleranzen von Korperfarben. *Farbe*, 42(4):207–220, 1996.

[61] ASTM International. Standard Practice for Calculation of Color Tolerances and Color Differences from Instrumentally Measured Color Coordinates, 7 2016. URL https://www.astm.org/d2244-16.html.

[62] Selig Hecht. The visual discrimination of intensity and the Weber-Fechner law. *The Journal of general physiology*, 7(2):235, 11 1924. ISSN 0022-1295. doi: 10.1085/jgp.7.2.235.

[63] International Electrotechnical Commission. Multimedia systems and equipment – Colour measurement and management – Part 2-1: Colour management – Default RGB colour space – sRGB, 1999. URL https://webstore.iec.ch/publication/6169.

[64] Multimedia Systems and Equipment - Colour Measurement and Management - Part 2-5: Colour Management - Optional RGB Colour Space - opRGB, 2007. URL https://webstore.iec.ch/publication/6175.

[65] Adobe Systems Inc. Adobe RGB (1998) Color Image Encoding. Technical report, Adobe Systems Incorporated, 2005. URL https://www.adobe.com/digitalimag/pdfs/AdobeRGB1998.pdf. Accessed: 2025-03-21.

[66] Chen Yang, Jie Wang, Nan Lyu, and Huw Lloyd. Comparison of digital photography and spectrometry for evaluating colour perception in humans and other trichromatic species. *Behavioral Ecology and Sociobiology*, 75(11):1–11, 10 2021. ISSN 0340-5443. doi: 10.1007/s00265-021-03071-8.

[67] Joice Jaqueline Kaschuk, Yazan Al Haj, Joaquin Valdez Garcia, Aleksi Kamppinen, Orlando J Rojas, Tiffany Abitbol, Kati Miettunen, and Jaana Vapaavuori. Processing factors affecting roughness, optical and mechanical properties of nanocellulose films for optoelectronics. *Carbohydrate Polymers*, 332:121877, 5 2024. ISSN 0144-8617. doi: 10.1016/j.carbpol.2024.121877.

[68] Monireh Imani, Ali Ghasemian, Mohammad Reza Dehghani-Firouzabadi, Elyas Afra, Maryam Borghei, Leena S Johansson, Patrick AC Gane, and Orlando J Rojas. Coupling nanofibril lateral size and residual lignin to tailor the properties of lignocellulose films. *Advanced Materials Interfaces*, 6(19):1900770, 8 2019. ISSN 2196-7350. doi: 10.1002/admi.201900770.

[69] Karl Alexander Henn, Nina Forsman, Tao Zou, and Monika Österberg. Colloidal Lignin Particles and Epoxies for Bio-Based, Durable, and Multiresistant Nanostructured Coatings. *ACS Applied Materials and Interfaces*, 13(29):34793–34806, 7 2021. ISSN 19448252. doi: 10.1021/acsami.1c06087.

[70] Hong Dong, James F. Snyder, Kristen S. Williams, and Jan W. Andzelm. Cation-induced hydrogels of cellulose nanofibrils with tunable moduli. *Biomacromolecules*, 14(9):3338–3345, 8 2013. ISSN 15257797. doi: 10.1021/bm400993f.

[71] Tobias Benselfelt, Malin Nordenström, Stefan B. Lindström, and Lars Wågberg. Explaining the Exceptional Wet Integrity of Transparent Cellulose Nanofibril Films in the Presence of Multivalent Ions—Suitable Substrates for Biointerfaces. *Advanced Materials Interfaces*, 6(13):1900333, 5 2019. ISSN 21967350. doi: 10.1002/admi.201900333.

[72] Kangyun Lee, Youngho Jeon, Dabum Kim, Goomin Kwon, Ung Jin Kim, Chaehwan Hong, Jin Woo Choung, and Jungmok You. Double-crosslinked cellulose nanofiber based bioplastic films for practical applications. *Carbohydrate Polymers*, 260:117817, 5 2021. ISSN 01448617. doi: 10.1016/j.carbpol.2021.117817.

[73] Asmetec GmbH. METOLIGHT® UV-Filter, 2018. URL https://www.asmetec-shop.de/asm_datenblaetter/METOLIGHT%20UV-Filter-DB-E.pdf. Accessed: 2024-05-29.

[74] Elena S Akulenko, Mahboubeh Hadadian, Maryam Esmaeilzadeh, Rustem Nizamov, and Kati Miettunen. Bottlenecks in Perovskite Solar Cell Recycling. *EU PVSEC 2023*, pages 001–004, 2023. doi: 10.4229/EUPVSEC2023/2BV.2.13.

[75] CR Osterwald and TJ McMahon. History of accelerated and qualification testing of terrestrial photovoltaic modules: A literature review. *Progress in Photovoltaics: Research and Applications*, 17(1):11–33, 2009. doi: 10.1002/pip.861.

[76] Ruuvi Innovations Ltd. RuuviTag Wireless Sensor, 2017. URL https://ruuvi.com/ruuvitag/. Accessed: 2025-03-04.

[77] David Kiermasch, Lidón Gil-Escrig, Henk J. Bolink, and Kristofer Tvingstedt. Effects of Masking on Open-Circuit Voltage and Fill Factor in Solar Cells. *Joule*, 3:16–26, 1 2019. ISSN 25424351. doi: 10.1016/j.joule.2018.10.016.

[78] Rustem Nizamov. Solar_cells_measurement_and_plotting, 2024. URL https://gitlab.com/mateng-utu/solar_cells_measurement_and_plotting. Accessed: 2024-02-16.

[79] Rustem Nizamov. RGB_recognition, 2024. URL https://gitlab.com/mateng-utu/RGB_recognition. Accessed: 2024-02-19.

[80] Karl Pearson and Alice Lee. On the laws of inheritance in man: I. Inheritance of physical characters. *Biometrika*, 2(4):357–462, 1903. doi: 10.2307/2331507.

[81] T Gambichler, Jan Laperre, and K Hoffmann. The European standard for sun-protective clothing: EN 13758. *Journal of the European Academy of Dermatology and Venereology*, 20(2):125–130, 1 2006. ISSN 0926-9959. doi: 10.1111/j.1468-3083.2006.01401.x.

[82] Standards Australia. Sun protective clothing—Evaluation and classification, 2020. URL https://www.standards.org.au/standards-catalogue/standard-details?designation=as-4399-2020.

[83] Yarong Li, Siyu Zhao, Yihan Li, Arthur J Ragauskas, Xueping Song, and Kai Li. Revealing the relationship between molecular weight of lignin and its color, UV-protecting property. *International Journal of Biological Macromolecules*, 223:1287–1296, 11 2022. ISSN 0141-8130. doi: 10.1016/j.ijbiomac.2022.11.067.

[84] L Ross C Barclay, Jennifer K Grandy, Heather D MacKinnon, Heather C Nichol, and Melinda R Vinqvist. Peroxidations initiated by lignin model compounds: investigating the role of singlet oxygen in photo-yellowing. *Canadian journal of chemistry*, 76(12):1805, 1998. ISSN 0008-4042. doi: 10.1139/cjc-76-12-1805.

[85] Angham G Hadi, Emad Yousif, Gamal A El-Hiti, Dina S Ahmed, Khudheyer Jawad, Mohammad Hayal Alotaibi, and Hassan Hashim. Long-term effect of ultraviolet irradiation on poly (vinyl chloride) films containing naproxen diorganotin (IV) complexes. *Molecules*, 24(13):2396, 6 2019. ISSN 1420-3049. doi: 10.3390/molecules24132396.

[86] Lucia Pucciarini, Federica Ianni, Valentina Petesse, Federica Pellati, Virginia Brighenti, Claudia Volpi, Marco Gargaro, Benedetto Natalini, Catia Clementi, and Roccaldo Sardella. Onion (Allium cepa L.) Skin: A rich resource of biomolecules for the sustainable production of colored biofunctional textiles. *Molecules*, 24(3):634, 2 2019. ISSN 14203049. doi: 10.3390/molecules24030634.

[87] Keith M Glassford and James R Chelikowsky. Structural and electronic properties of titanium dioxide. *Physical Review B*, 46(3):1284, 7 1992. ISSN 0163-1829. doi: 10.1103/physrevb.46.1284.

[88] Iikpoemugh Elo Imiete, Luca Giannini, Luciano Tadiello, Marco Orlandi, and Luca Zoia. The effect of sulfate half-ester groups on the mechanical performance of cellulose nanocrystal-natural rubber composites. *Cellulose*, 30(14):8929–8940, 2023. doi: doi.org/10.1007/s10570-023-05432-0.

[89] Mahboubeh Hadadian, Jan-Henrik Smått, and Juan-Pablo Correa-Baena. The role of carbon-based materials in enhancing the stability of perovskite solar cells. *Energy & Environmental Science*, 13 (5):1377–1407, 2020. ISSN 1754-5692. doi: 10.1039/c9ee04030g.

[90] Ganbaatar Tumen-Ulzii, Chuanjiang Qin, Toshinori Matsushima, Matthew R Leyden, Umamahesh Balijipalli, Dino Klotz, and Chihaya Adachi. Understanding the degradation of Spiro-OMeTAD-based perovskite solar cells at high temperature. *Solar RRL*, 4(10):2000305, 8 2020. ISSN 2367-198X. doi: 10.1002/solr.202000305.

[91] Sean P Dunfield, Lyle Bliss, Fei Zhang, Joseph M Luther, Kai Zhu, Maikel FAM van Hest, Matthew O Reese, and Joseph J Berry. From defects to degradation: a mechanistic understanding of degradation in perovskite solar cell devices and modules. *Advanced Energy Materials*, 10(26): 1904054, 3 2020. ISSN 1614-6832. doi: 10.1002/aenm.201904054.

TURUN
YLIOPISTO
UNIVERSITY
OF TURKU

Painosalama, Turku, Finland 2025

ISBN 978-952-02-0327-6 (PRINT)
ISBN 978-952-02-0328-3 (PDF)
ISSN 2736-9390 (PRINT)
ISSN 2736-9684 (ONLINE)